SPRINGER BRIEFS IN
APPLIED SCIENCES AND TECHNOLOGY

Pavle Boškoski
Andrej Debenjak
Biljana Mileva Boshkoska

Fast Electrochemical Impedance Spectroscopy

As a Statistical Condition Monitoring Tool

Springer

SpringerBriefs in Applied Sciences and Technology

Series editor

Janusz Kacprzyk, Polish Academy of Sciences, Systems Research Institute, Warsaw, Poland

SpringerBriefs present concise summaries of cutting-edge research and practical applications across a wide spectrum of fields. Featuring compact volumes of 50 to 125 pages, the series covers a range of content from professional to academic. Typical publications can be:

- A timely report of state-of-the art methods
- An introduction to or a manual for the application of mathematical or computer techniques
- A bridge between new research results, as published in journal articles
- A snapshot of a hot or emerging topic
- An in-depth case study
- A presentation of core concepts that students must understand in order to make independent contributions

SpringerBriefs are characterized by fast, global electronic dissemination, standard publishing contracts, standardized manuscript preparation and formatting guidelines, and expedited production schedules.

On the one hand, **SpringerBriefs in Applied Sciences and Technology** are devoted to the publication of fundamentals and applications within the different classical engineering disciplines as well as in interdisciplinary fields that recently emerged between these areas. On the other hand, as the boundary separating fundamental research and applied technology is more and more dissolving, this series is particularly open to trans-disciplinary topics between fundamental science and engineering.

Indexed by EI-Compendex and Springerlink

More information about this series at http://www.springer.com/series/8884

Pavle Boškoski · Andrej Debenjak
Biljana Mileva Boshkoska

Fast Electrochemical Impedance Spectroscopy

As a Statistical Condition Monitoring Tool

Springer

Pavle Boškoski
Department of Systems and Control
Jožef Stefan Institute
Ljubljana
Slovenia

Andrej Debenjak
Department of Systems and Control
Jožef Stefan Institute
Ljubljana
Slovenia

Biljana Mileva Boshkoska
Faculty of Information Studies in Novo mesto
Novo mesto
Slovenia

ISSN 2191-530X ISSN 2191-5318 (electronic)
SpringerBriefs in Applied Sciences and Technology
ISBN 978-3-319-53389-6 ISBN 978-3-319-53390-2 (eBook)
DOI 10.1007/978-3-319-53390-2

Library of Congress Control Number: 2017933548

Printed on acid-free paper

This Springer imprint is published by Springer Nature
The registered company is Springer International Publishing AG
The registered company address is: Gewerbestrasse 11, 6330 Cham, Switzerland

Preface

This book addresses the practical issues of electrochemical impedance spectroscopy (EIS), which arise when the technique is employed as an online condition monitoring tool for electrochemical devices. The main focus is the proposed fast EIS technique, with a special application on proton exchange membrane (PEM) fuel cells. The applicability of the method is presented on various types of electrochemical devices, such as a Lithium-ion battery, a Li-S cell, and an industrial grade PEM fuel cell.

The first part of the book addresses the theoretical aspects of the fast EIS technique. It includes topics on stochastic excitation signals, time–frequency signal processing, and statistical analysis of the impedance measurements. Based on this, a unit-free condition indicator is designed, whose value directly reflects the state of health of the electrochemical device.

In the second part, an application of the fast EIS technique for condition monitoring is proposed. The material addresses each point in the process of designing and commissioning a condition monitoring system. Based on the derived probability density function of the impedance components, alarm thresholds are specified based on the desired probability of false alarm. Finally, the overall performance of such a condition monitoring system is evaluated on an industrial-grade PEM fuel cell system for detecting and evaluating various water management faults.

The final chapter of the book provides the necessary link for practical applications by proposing hardware components for an embedded condition monitoring system that consists of a multichannel high-resolution voltage monitor and a DC–DC converter capable of generating the required excitation signals. Special attention is given to the difficulties of accurate measurements of low voltage values superimposed on high potentials as well as energy efficiency of the DC–DC converter. The provided hardware implementation together with the detailed methodology represent a solid base for building an effectual condition monitoring system.

Unlike many other publications addressing the issues of electrochemical impedance spectroscopy that only cover the theoretical aspect, this book additionally provides practical guidelines for implementation as well as for commissioning and exploitation of the results. The presentation of the proposed fast EIS technique

significantly focuses on difficulties that arise from real-world implementations. The material offers a balanced overview of both the theoretical and practical aspects of performing EIS and online condition monitoring of electrochemical devices, thus offering new, valuable information attractive to both researchers and engineers.

Ljubljana, Slovenia
September 2016

Pavle Boškoski
Andrej Debenjak
Biljana Mileva Boshkoska

Acknowledgements

First and foremost, the authors would like to thank Janko Petrovčič for his selfless sharing of his passion for engineering, knowledge, and commitment to perfection. Our sincere thanks also go to the other members of the Department of Systems and Control, Jožef Stefan Institute, Slovenia, for their help and support, especially Đani Juričić, Vladimir Jovan, Bojan Musizza, and Stanislav Černe.

The authors acknowledge the financial support of the Slovenian Research Agency through the Research Programme P2-0001 and Research Project L2-7663. The authors also thank the Centre of Excellence for Low-carbon Technologies—CO NOT, financed by the Slovenian Ministry of Higher Education, Science and Technology and co-financed by the European Regional Development Fund.

Contents

Acronyms

BoP	Balance of plant
CAN	Controller area network
CDF	Cumulative distribution function
CI	Condition indicator
CM	Condition monitoring
CWT	Continuous wavelet transform
DC–DC	Direct current to direct current
EIS	Electrochemical impedance spectroscopy
FCVM	Fuel cell voltage monitor
FFT	Fast Fourier transform
FNAC	Fully nested Archimedean copula
Li-ion	Lithium-ion
Li-S	Lithium-sulphur
MOSFET	Metal-oxide-semiconductor field effect transistor
PDF	Probability density function
PEM	Proton exchange membrane
PFA	Probability of false alarm
PRBS	Pseudo-random binary sequence
PWM	Pulse-width modulation

Chapter 1
Introduction

Electrochemical impedance spectroscopy (EIS) is a technique used in various fields of electrochemistry. It is frequently employed for the characterisation and diagnostics of electrochemical devices [1]. Such devices involve a combination of electrochemical, electric, transportation, and thermodynamic processes. The true power of EIS lies in its capability to recognise and to analyse the majority of the inherent processes of an electrochemical device solely by employing directly measurable quantities, such as voltage and electric current.

EIS is an *active* characterisation tool that requires external excitation of the electrochemical device under test. Traditionally, small-amplitude sinusoids are employed as excitation signals [1–3]. With such excitation signals, one can assume time-invariance and linearity of the electrochemical device's dynamics around the operating point [4]. Under such an assumption, sinusoidal current excitation with frequency f_0 results in sinusoidal voltage change with particular amplitude $|V_0|$ and phase φ at the same frequency f_0. The ratio between the output voltage and the excitation current in the frequency domain is the impedance of the device at the excited frequency f_0.

Single frequency sine excitation provides precise impedance measurements[1] because all the energy of the excitation signal is condensed at a single frequency. The price for such a performance is the required time for measurements. This drawback becomes even more prominent in cases when the impedance characterisation is performed either at very low frequencies or over a wide frequency band. The focal point of this book is to provide an enhancement to the EIS technique that overcomes the measurement time issues while at the same time sufficiently preserving accurate

[1] In the concept of information theory, measurement is defined as a set of observations that reduces uncertainty where the result is expressed as a quantity [5]. Such a definition of a measurement process makes the distinction between a measurement and estimation somewhat vague. Throughout this book the term measurement, in the context of information theory, is used for describing the process of determining impedance values by means of EIS.

P. Boškoski et al., *Fast Electrochemical Impedance Spectroscopy*,
SpringerBriefs in Applied Sciences and Technology,
DOI 10.1007/978-3-319-53390-2_1

impedance measurements. Such an enhancement is especially convenient in cases when there are hard time constraints for performing EIS. Typical examples include online characterisation and condition monitoring of electrochemical devices.

The issues of the EIS have already been addressed by numerous authors. The proposed approaches predominantly target the design of excitation signals, whereas the signal processing is limited to Fourier transform based methods. The most prominent approaches include multi-sine excitation [6, 7], broadband frequency-amplitude optimisation [8], and (pseudo-)stochastic signals [9].

The fast EIS technique presented in this book employs discrete random binary sequence (DRBS) as an excitation signal waveform and continuous wavelet transform (CWT) with complex Morlet wavelet as a signal processing tool [10]. The combination of DRBS and CWT offers several advantages. First, the DRBS waveform can be easily generated as a pseudo-random binary sequence (PRBS). Secondly, compared to other time-frequency methods, CWT with Morlet wavelet provides superior time-frequency resolution. This is especially important when impedance has to be measured at low frequencies. Additionally, the time required for performing EIS over a wide frequency band is substantially shorter than with the classical approaches. Finally, CWT with complex Morlet wavelet can be implemented in a computationally efficient manner, which is convenient for embedded applications.

In addition to the fast EIS technique itself, this book also provides:

- An in-depth analysis for optimal parameter tuning of the Morlet wavelet and PRBS waveform. These parameters are essential for the accuracy of the fast EIS technique.
- A comprehensive statistical analysis of the measured impedance characteristics by employing the framework of complex random variables. As a result, the corresponding probability density functions (PDFs) of the measured impedance are derived in a closed form.
- A framework for condition monitoring of electrochemical devices based on fast EIS and its statistical properties. The proposed condition monitoring approach fuses the EIS information into an overall condition indicator. The main benefit of this approach are significantly simplified commissioning procedures and enhanced maintenance decision support.
- A design of an embedded condition monitoring system for an industrial grade proton exchange membrane (PEM) fuel cell system built on top of the fast EIS technique.
- Case studies of impedance measurements for RC circuits, lithium-ion (Li-ion) batteries, lithium-sulphur (Li-S) cells, and PEM fuel cells.
- An application of condition monitoring on an industrial PEM fuel cell system.

1.1 EIS as a Tool for Condition Monitoring

According to Isermann and Ballé [11], the term condition monitoring is defined as follows:

> *A continuous real-time task of determining the conditions of a physical system, by recording information, recognising and indicating anomalies in the behaviour.*

In the context of electrochemical devices, the degradation phenomena that affect the system's condition can be grouped in three broad categories [12, 13]:

(i) phenomena affecting electrodes, such as ageing and corrosion [14–21],
(ii) phenomena affecting chemical and physical composition of the constituent parts, such as particle size growth [22], dendrite growth mechanisms [23], membrane poisoning [18–21], water management faults (i.e., flooding of gas channels and membrane drying) [24–26], etc., and
(iii) mechanical degradation.

These degradation phenomena have a profound effect on the impedance characteristic of an electrochemical device, making the EIS technique a viable candidate for condition monitoring [2, 27–31].

The EIS technique has already been applied as a condition monitoring tool for various electrochemical devices, such as PEM fuel cells [27, 32–36] and lithium based batteries [37, 38]. In comparison to other diagnostic methods, EIS is less invasive, is capable of differentiating among different types of faults, and is able to distinguish various causes for condition deterioration. Moreover, it can be performed during operation of an electrochemical device with only a slight amount of perturbation, which is of great practical value in real-world applications.

Despite the apparent benefits, current EIS implementations have four major drawbacks:

1. The application of sine waves as excitation signals is time-consuming, hence inappropriate for online condition monitoring.
2. Determining appropriate diagnostics threshold values requires a priori characterisation of a fuel cell, which in many cases is infeasible.
3. Performing EIS characterisation over a large number of frequencies results in a feature set with large cardinality.
4. EIS is performed by using expensive and sophisticated equipment that is predominantly designed for laboratory use.

This book proposes a solution for all four issues. The focal point, the fast EIS technique, provides a way for impedance characterisation over a wide frequency band in a timely manner. By using DRBS as excitation signal, the statistical properties of the impedance values can be specified in a closed form. Since the impedance values are usually regarded as feature values, this allows straightforward calculation of the diagnostics thresholds based on the desired probability of false alarm (PFA) [39]. Having specified the features' statistical properties in a closed form can be exploited for fusing the information from the multidimensional feature set into a

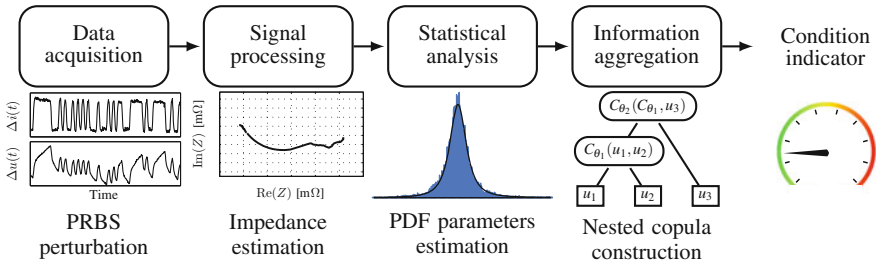

Fig. 1.1 Schematic representation of the complete condition monitoring process

single condition indicator. The information fusion technique used in this book is based on copula functions [40]. The complete process, from the data acquisition to the calculation of the condition indicator, is shown in Fig. 1.1.

The last building block of the proposed condition monitoring process is a hardware setup that allows simultaneous excitation of the electrochemical device and data acquisition [41, 42]. For true online operation, such a setup is capable of performing both tasks without affecting the normal operation of the tested electrochemical device. The developed hardware consists of a fuel cell voltage monitor coupled with an excitation enabling DC-DC converter.

1.2 Book Structure

This book has two distinctive parts. In the first part, the theoretical background of the proposed fast EIS technique is presented. Chapter 2 contains the algorithm for selecting the appropriate structure of the DRBS excitation as well as the signal processing method based on CWT with complex Morlet wavelet. Chapter 3 presents the complete statistical analysis of the estimated impedance components. It provides analytical derivation of the corresponding probability density functions and cumulative distribution functions. The applicability of the proposed fast EIS technique is shown on several test cases presented in Chap. 4.

The second part of this book presents methods for applying the fast EIS technique for the purpose of condition monitoring and the corresponding results. Chapter 5 presents the theoretical derivation of the described condition indicator and method for determining optimal diagnostic thresholds based on PFA. The results of the evaluation of the proposed condition monitoring algorithm are presented in Chap. 6. Finally, Chap. 7 presents the developed hardware platform for condition monitoring and power conditioning.

References

1. Lasia, Andrzej. 2014. *Electrochemical impedance spectroscopy and its applications*. New York: Springer. doi:10.1007/978-1-4614-8933-7.
2. Yuan, Xiao-Zi, Chaojie Sons, Haijiang Wang, and Jiujun Zhang. 2010. *Electrochemical impedance spectroscopy in PEM fuel cells, fundamentals and applications*. London: Springer.
3. Orazem, Mark E., and Bernard Tribollet. 2008. *Electrochemical impedance spectroscopy*. New Jersey: Wiley. doi:10.1002/9780470381588.
4. Schoukens, J., M. Vaes, and R. Pintelon. 2016. Linear system identification in a nonlinear setting: Nonparametric analysis of the nonlinear distortions and their impact on the best linear approximation. *IEEE Control Systems* 36 (3): 38–69. doi:10.1109/MCS.2016.2535918.
5. Hubbard, Douglas W. 2014. *How to measure anything*. New Jersey: Wiley.
6. Brunetto, Carmelo, Antonino Moschetto, and Giuseppe Tina. 2008. PEM fuel cell testing by electrochemical impedance spectroscopy. *Electric Power System Research* 79: 17–26.
7. Wasterlain, Sébastien, Denis Candusso, Fabien Harel, Daniel Hissel, and Xavier François. 2011. Development of new test instruments and protocols for the diagnostic of fuel cell stacks. *Journal of Power Sources* 196 (12): 5325–5333.
8. de Beer, Chris, Paul S. Barendse, and Pragasen Pillay. 2015. Fuel cell condition monitoring using optimized broadband impedance spectroscopy. *IEEE Transactions on Industrial Electronics* 62 (8): 5306–5316.
9. Pintelon, Rik, and Johan Schoukens. 2001. *System identification: A frequency domain approach*. New York: IEEE Press.
10. Debenjak, Andrej., Pavle Boškoski, Bojan Musizza, Janko Petrovčič, and Đani Juričić. 2014. Fast measurement of proton exchange membrane fuel cell impedance based on pseudo-random binary sequence perturbation signals and continuous wavelet transform. *Journal of Power Sources* 254: 112–118. doi:10.1016/j.jpowsour.2013.12.094.
11. Isermann, Rolf., and P. Ballé. . 1997. Trends in the application of model-based fault detection and diagnosis of technical processes. *Control Engineering Practice* 5 (5): 709–719. doi:10.1016/S0967-0661(97)00053-1.
12. de Bruijn, F.A., V.A.T. Dam, and G.J.M. Janssen. 2008. Review: Durability and degradation issues of PEM fuel cell components. *Fuel Cells* 8 (1): 3–22. doi:10.1002/fuce.200700053.
13. Schmittinger, Wolfgang, and Ardalan Vahidi. 2008. A review of the main parameters influencing long-term performance and durability of pem fuel cells. *Journal of Power Sources* 180 (1): 1–14.
14. Colón-Mercado, Héctor R., and Branko N. Popov. 2006. Stability of platinum based alloy cathode catalysts in PEM fuel cells. *Journal of Power Sources* 155 (2): 253–263. doi:10.1016/j.jpowsour.2005.05.011.
15. Borup, Rod, Jeremy Meyers, Bryan Pivovar, Yu Seung Kim, Rangachary Mukundan, Nancy Garland, Deborah Myers, Mahlon Wilson, Fernando Garzon, David Wood, Piotr Zelenay, Karren More, Ken Stroh, Tom Zawodzinski, James Boncella, James E. McGrath, Minoru Inaba, Kenji Miyatake, Michio Hori, Kenichiro Ota, Zempachi Ogumi, Seizo Miyata, Atsushi Nishikata, Zyun Siroma, Yoshiharu Uchimoto, Kazuaki Yasuda, Ken-ichi Kimijima, and Norio Iwashita. 2007. Scientific aspects of polymer electrolyte fuel cell durability and degradation. *Chemical Reviews* 107 (10): 3904–3951. doi:10.1021/cr0501821.
16. Yu, Paul T., Zhongyi Liu, and Rohit Makharia. 2013. Investigation of carbon corrosion behavior and kinetics in proton exchange membrane fuel cell cathode electrodes. *Journal of The Electrochemical Society* 160 (6): F645–F650.
17. Fairweather, Joseph D., Dusan Spernjak, Adam Z. Weber, David Harvey, Silvia Wessel, Daniel S. Hussey, David L. Jacobson, Kateryna Artyushkova, Rangachary Mukundan, and Rodney L. Borup. 2013. Effects of cathode corrosion on through-plane water transport in proton exchange membrane fuel cells. *Journal of The Electrochemical Society* 160 (9): F980–F993. doi:10.1149/2.024309jes.

18. Farrell, C.G., C.L. Gardner, and M. Ternan. 2007. Experimental and modelling studies of CO poisoning in PEM fuel cells. *Journal of Power Sources* 171 (2): 282–293. doi:10.1016/j.jpowsour.2007.07.006.
19. Cheng, Xuan, Zheng Shi, Lu Nancy Glass, Jiujun Zhang Zhang, Datong Song, Zhong-Sheng Liu, Haijiang Wang, and Jun Shen. 2007. A review of PEM hydrogen fuel cell contamination: Impacts, mechanisms, and mitigation. *Journal of Power Sources* 165 (2): 739–756.
20. Yan, Wei-Mon, Hsin-Sen Chu, Lu Meng-Xi, Fang-Bor Weng, Guo-Bin Jung, and Chi-Yuan Lee. 2009. Degradation of proton exchange membrane fuel cells due to CO and CO_2 poisoning. *Journal of Power Sources* 188 (1): 141–147.
21. Postole, Georgeta, and Aline Auroux. 2011. The poisoning level of Pt/C catalysts used in PEM fuel cells by the hydrogen feed gas impurities: The bonding strength. *International Journal of Hydrogen Energy* 36 (11): 6817–6825. doi:10.1016/j.ijhydene.2011.03.018.
22. Song, Juhyun, and Martin Z. Bazant. 2013. Effects of nanoparticle geometry and size distribution on diffusion impedance of battery electrodes. *Journal of The Electrochemical Society* 160 (1): A15–A24. doi:10.1149/2.023301jes.
23. Steiger, Jens. 2015. *Mechanisms of Dendrite Growth in Lithium Metal Batteries*. PhD thesis, Fakultät für Maschinenbau Karlsruher Institut für Technologie.
24. Li, Hui, Yanghua Tang, Zhenwei Wang, Zheng Shi, Wu Shaohong, Datong Song, Jianlu Zhang, Khalid Fatih, Jiujun Zhang, Haijiang Wang, Zhongsheng Liu, Rami Abouatallah, and Antonio Mazza. 2008. A review of water flooding issues in the proton exchange membrane fuel cell. *Journal of Power Sources* 178 (1): 103–117. doi:10.1016/j.jpowsour.2007.12.068.
25. Yousfi-Steiner, Nadia, Philippe Moçotéguy, D. Candusso, D. Hissel, A. Hernandez, and A. Aslanides. 2008. A review on PEM voltage degradation associated with water management: Impacts, influent factors and characterization. *Journal of Power Sources* 183 (1): 260–274.
26. Ous, T., and C. Arcoumanis. 2013. Degradation aspects of water formation and transport in proton exchange membrane fuel cell: A review. *Journal of Power Sources* 240: 558–582. doi:10.1016/j.jpowsour.2013.04.044.
27. Yuan, Xiao-Zi, Haijiang Wang, Jian Colin Sun, and Jiujun Zhang. 2007. AC impedance technique in PEM fuel cell diagnosis - A review. *International Journal of Hydrogen Energy* 32: 4365–4380.
28. Wu, Jinfeng, Xiao Zi Yuan, Haijiang Wang, Mauricio Blanco, Jonathan J. Martin, and Jiujun Zhang. 2008. Diagnostic tools in PEM fuel cell research: Part I electrochemical techniques. *International Journal of Hydrogen Energy* 33 (6): 1735–1746.
29. Petrone, R., Z. Zheng, D. Hissel, M.C. Péra, C. Pianese, M. Sorrentino, M. Becherif, and N. Yousfi-Steiner. 2013. A review on model-based diagnosis methodologies for PEMFCs. *International Journal of Hydrogen Energy* 38 (17): 7077–7091. doi:10.1016/j.ijhydene.2013.03.106.
30. Zheng, Z., R. Petrone, M.C. Péra, D. Hissel, M. Becherif, C. Pianese, N. Yousfi-Steiner, and M. Sorrentino. 2013. A review on non-model based diagnosis methodologies for PEM fuel cell stacks and systems. *International Journal of Hydrogen Energy* 38 (21): 8914–8926. doi:10.1016/j.ijhydene.2013.04.007.
31. Niya, Seyed Mohammad Rezaei, and Mina Hoorfar. 2013. Study of proton exchange membrane fuel cells using electrochemical impedance spectroscopy technique - A review. *Journal of Power Sources* 240: 281–293. doi:10.1016/j.jpowsour.2013.04.011.
32. Fouquet, N., C. Doulet, C. Nouillant, G. Dauphin-Tanguy, and B. Ould-Bouamama. 2005. Model based PEM fuel cell state-of-health monitoring via AC impedance measurements. *Journal of Power Sources* 159: 905–913.
33. Merida, W., D.A. Harrington, J.M. Le Canut, and G. McLean. 2006. Characterisation of proton exchange membrane fuel cell (PEMFC) failures via electrochemical impedance spectroscopy. *Journal of Power Sources* 161 (1): 264–274. doi:10.1016/j.jpowsour.2006.03.067.
34. Le Canut, Jean-Marc, Rami M. Abouatallah, and David A. Harrington. 2006. Detection of membrane drying, fuel cell flooding, and anode catalyst poisoning on PEMFC stack by electrochemical impedance spectroscopy. *Journal of The Electrochemical Society* 153: A857–A864.

35. Debenjak, Andrej, Matej Gašperin, Boštjan Pregelj, Maja Atanasijević-Kunc, Janko Petrovčič, and Vladimir Jovan. 2013. Detection of flooding and drying inside a PEM fuel cell stack. *Strojniški vestnik - Journal of Mechanical Engineering* 59 (1): 56–64. doi:10.5545/sv-jme.2012.640.
36. Cruz-Manzo, Samuel, and Rui Chen. 2013. An electrical circuit for performance analysis of polymer electrolyte fuel cell stacks using electrochemical impedance spectroscopy. *Journal of The Electrochemical Society* 160 (10): F1109–F1115. doi:10.1149/2.025310jes.
37. Itagaki, Masayuki, Keiichirou Honda, Yoshinao Hoshi, and Isao Shitanda. 2015. In-situ EIS to determine impedance spectra of lithium-ion rechargeable batteries during charge and discharge cycle. *Journal of Electroanalytical Chemistry* 737: 78–84. doi:10.1016/j.jelechem.2014.06.004. (Special issue in honor of Bernard Tribollet).
38. Thanapalan, K., M. Bowkett, J. Williams, M. Hathway, and T. Stockley. 2014. Advanced EIS techniques for performance evaluation of Li-ion cells. *IFAC Proceedings Volumes* 47 (3): 8610–8615. doi:10.3182/20140824-6-ZA-1003.02463. (19th IFAC World Congress).
39. Boškoski, Pavle, and Andrej Debenjak. 2014. Optimal selection of proton exchange membrane fuel cell condition monitoring thresholds. *Journal of Power Sources* 268: 692–699.
40. Mileva Boshkoska, Biljana, Pavle Boškoski, Andrej Debenjak, and Đani Juričić. 2015. Dependence among complex random variables as a fuel cell condition indicator. *Journal of Power Sources* 284: 566–573. doi:10.1016/j.jpowsour.2015.03.044.
41. Andrej Debenjak, Janko Petrovčič, Pavle Boškoski, Bojan Musizza, and Đani Juričić. 2015. Fuel cell condition monitoring system based on interconnected DC-DC converter and voltage monitor. *IEEE Transactions on Industrial Electronics*, 62 (8): 5293–5305, 2015. 10.1109/TIE.2015.2434792.
42. Pregelj, Boštjan, Andrej Debenjak, Gregor Dolanc, and Janko Petrovčič. 2017. A diesel-powered fuel cell APU – reliability issues and mitigation approaches. *IEEE Transactions on Industrial Electronics*, PP (99): 1–11.

Chapter 2
Fast Electrochemical Impedance Spectroscopy

EIS is a widely adopted method for the characterisation and diagnostics of electrochemical devices [1–5]. The impedance characteristic is measured at a fixed operating point defined by current I_{dc}. The conventional EIS approach utilises a sinusoidal waveform as an excitation signal (i.e., single-sine approach) [6, 7]. In order to measure the impedance in a frequency band of interest at frequencies $f_i \in \Omega$, the procedure of applying single-sine electric current excitation has to be repeated multiple times for each frequency f_i. Assuming linearity of the electrochemical device's dynamics around a fixed operating point, the device responds with sinusoidal voltage change with the same frequency f_i and particular amplitude and phase. The impedance of the electrochemical device at frequency f_i is the ratio between voltage and current in the frequency domain. Commonly, the transformation from time to frequency domain is performed by fast Fourier transform (FFT). Consequently, the impedance is the ratio between the complex FFT coefficients.

With the single-sine excitation approach, the impedance characteristic of an electrochemical device is constructed at discrete frequencies $f_i \in \Omega$. The approach provides precise impedance measurements because all of the energy of the excitation signal is condensed at a single frequency only. Such an excitation provides maximal perturbation at the selected frequency f_i at the expense of lengthy measurements.

Despite the simplicity of the excitation and the signal processing step, performing EIS with such an approach is inefficient. First, applying single-sine excitation signals is time consuming, which is tightly linked to the lower frequency limit of the frequency band. Secondly, the application of FFT as a signal processing tool provides solely time average impedance estimates thus failing to provide any additional information required for further processing, for instance confidence intervals. Consequently, there is an apparent need for an improved EIS approach that will allow shorter measurement time while at the same time providing richer output than simply time-averaged values.

P. Boškoski et al., *Fast Electrochemical Impedance Spectroscopy*,
SpringerBriefs in Applied Sciences and Technology,
DOI 10.1007/978-3-319-53390-2_2

Addressing these two issues, this chapter presents an approach based on DRBS as an excitation signal and CWT with Morlet mother wavelet as a signal processing tool. The DRBS is well-established as an excitation signal in the field of system identification since it has white-noise-like spectral properties in a predefined frequency band. The main advantage of using DRBS as excitation compared to the conventional one, is shorter probing time. Furthermore, with properly tuned parameters, CWT provides optimal time-frequency resolution. Consequently, it provides reliable impedance measurements along the entire frequency band. Additionally, it yields statistical information about confidence intervals of the impedance measurements.

The application of a more complex excitation signal, such as the proposed DRBS, offers several advantages. First, the time required for performing EIS is significantly shorter.[1] Secondly, as the electrochemical device is perturbed by the broadband signal, the value of impedance can be computed at any frequency of interest by properly adjusting the parameters of CWT and DRBS. Additionally, the frequency-domain representation of the Morlet wavelet exists in a closed form, therefore the required time-domain convolution can be efficiently conducted in the frequency-domain as a multiplication. This implies a significant practical advantage for the implementation of the algorithm on embedded systems, where the computation resources are limited.

Employing the fast EIS technique in the optimal manner requires proper tuning of the CWT parameters. Additionally, DRBS excitation is usually implemented as a PRBS whose parameters also affect the overall performance of the fast EIS technique. For PRBS, these parameters include the order n, sampling period Δt, and amplitude a. For the CWT with the Morlet mother wavelet, the key parameters are the length of the signals, central frequency ω_0, cone of influence e. In what follows, methods for optimal parameter selection and computationally efficient implementation of the proposed fast EIS technique are presented.

2.1 Discrete Random Binary Sequence

The fundamentals of the DRBS origin from *continuous-time random binary signal* has the following two properties:

- the value of the signal can either be a or $-a$, and
- switch from one value to the other can occur at any given time.[2]

However, for the implementation and signal processing by means of digital computers, the *discrete random binary sequence* is much more convenient. In contrast to the continuous-time random binary signal, the changes in value of the discrete one occur only at discrete points in time $k\lambda$ ($k \in \mathbb{N}^0$), where λ is the length of the time interval. Time interval λ is the time between two consecutive points where the signal

[1] For detailed comparison see results presented in Sect. 4.4.

[2] In a given period of time, the probability of the number of changes of the signal's value is distributed according to Poisson distribution [8, pp. 161–162].

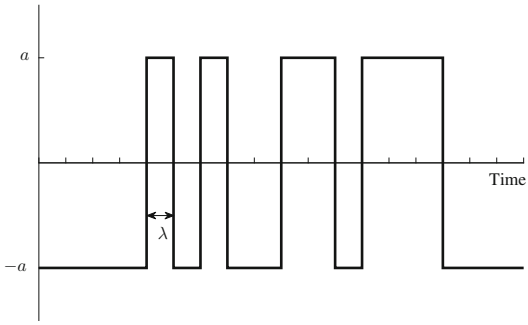

Fig. 2.1 DRBS waveform

can change its value. The generating process for DRBS has the following form:

$$X(t) = \sum_n a_n p(t - n\lambda - \alpha), \alpha \sim \mathscr{U}[0, \lambda], \tag{2.1}$$

where $p(t)$ is the probability describing the binary change of amplitude a and α is random phase shift, making process $X(t)$ stationary. A single realisation of the DRBS defined by (2.1) is shown in Fig. 2.1.

The power spectral density of the DRBS defined by (2.1) is

$$\Phi_X^d(\omega) = a^2\lambda \left| \frac{\sin\left(\frac{\omega\lambda}{2}\right)}{\frac{\omega\lambda}{2}} \right|^2. \tag{2.2}$$

The power spectral density shown in Fig. 2.2 has zeros exactly at integer multiples of the frequency $1/\lambda$. Since the beneficial properties of the DRBS are present only in a limited frequency band, the signal has to be applied with care. Out of this band, the device under examination is perturbed with substantially lower energy and thus it can not be characterised (identified) with sufficient accuracy. The useful frequency

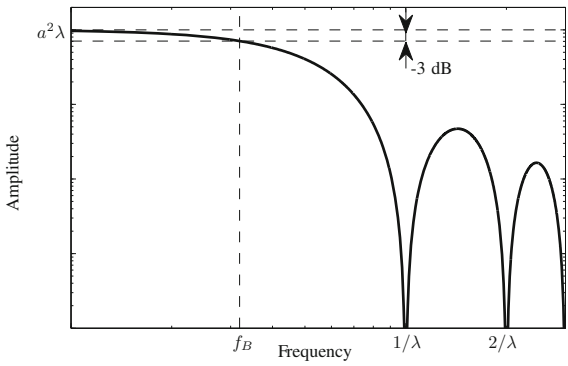

Fig. 2.2 Power spectral density of the DRBS

band f_B is approximately determined by the -3 dB frequency limit as [9]

$$f_B = \frac{1}{3\lambda}. \tag{2.3}$$

Pseudo-Random Binary Sequence

Mainly due to the ease of implementation, the PRBS is most often employed as a sufficiently close approximation of the DRBS. According to Ljung [10], PRBS is a periodic and deterministic signal with white-noise-like properties. As such, it is highly appropriate as an input test (i.e., excitation) signal for system identification purposes.[3] The maximum length PRBS is generated by employing feedback shift registers [8, 9]. The PRBS is characterised by

- the amplitude a, and
- the order n of the shift register,
- the length of the time interval λ.

The order n of the underlying shift register determines the maximum length N of the PRBS. In other words, it determines the number of discrete points in time when the PRBS signal can change its value. The relation between the order and the maximum length is as follows:

$$N = 2^n - 1. \tag{2.4}$$

Order n, together with the length of the time interval λ, defines the maximum length period T_p of the PRBS:

$$T_p = (2^n - 1)\lambda = N\lambda. \tag{2.5}$$

The discrete power spectrum density Φ^d of the maximum length PRBS with amplitude a and maximum length N is

$$\begin{aligned} \Phi^d(m) &= a^2 - \frac{a^2}{N}\sum_{\tau_i=1}^{N-1} e^{-j\frac{2\pi}{N}m\tau_i} \\ &= \begin{cases} \frac{a^2}{N} & m = 0 \\ \frac{a^2(N+1)}{N} & 0 < m < N. \end{cases} \end{aligned} \tag{2.6}$$

Therefore, the power spectrum of a periodic PRBS with the length of the time interval λ is

$$\Phi^p\left(m\frac{2\pi}{N\lambda}\right) = \frac{1}{N}\Phi^d(m)\left|\frac{\sin\frac{m\pi}{N}}{\frac{m\pi}{N}}\right|^2. \tag{2.7}$$

The power spectral density can be obtained by dividing the power spectrum (2.7) by $1/T$ as

[3] From the *systems theory's* point of view, EIS is a system identification technique.

$$\begin{aligned}\Phi^d(\omega) &= \frac{T}{N}\Phi^d(m)\left|\frac{\sin\frac{m\pi}{N}}{\frac{m\pi}{N}}\right|^2_{\omega=\frac{2\pi m}{T}} \\ &= \lambda\Phi^d(m)\left|\frac{\sin\frac{\omega\lambda}{2}}{\frac{\omega\lambda}{2}}\right|^2.\end{aligned} \tag{2.8}$$

By letting $N \to \infty$, the periodic PRBS signal becomes a signal with properties of the DRBS. The relation (2.6) becomes

$$\Phi^d(m) = a^2. \tag{2.9}$$

As a result, the power spectral density of the PRBS (2.8) becomes the same as the power spectral density of the DRBS (2.2).

It should be noted that PRBS is generated through a deterministic state machine and as such it can be created without any random number generator. However, true random generators are not rareness anymore in present-day microprocessors and therefore one can directly employ DRBS. The remaining analysis is valid regardless of whether PRBS or DRBS is used as an excitation signal.

2.2 Frequency Analysis

The straightforward way of extracting impedance data from the signals is by calculating the ratio of the Fourier transform of the excitation electric current and the resulting voltage as [7]

$$Z(j\omega) = \frac{U(j\omega)}{I(j\omega)} = \frac{\mathscr{F}\{u(t)\}}{\mathscr{F}\{i(t)\}}. \tag{2.10}$$

The resulting complex impedance characteristic $Z(j\omega)$[4] is incomplete. The biggest deficiency when calculating impedance using (2.10) is the lack of variance i.e., a general estimation of confidence intervals. The Fourier transform provides only time averaged amplitude and phase for the calculated frequencies. This issue can be resolved by employing time-frequency signal processing methods.

2.3 Time-Frequency Analysis

Unlike Fourier analysis, which allows only time-averaged analysis, the time-frequency methods enable analysis in a two dimensional time-frequency

[4]Throughout this book, the symbol j is used instead of $i = \sqrt{-1}$, since in the area of electrical engineering the symbol i is established as a symbol for electrical current.

plane [11]. As a result, the signal's spectral evolution in time can be observed. Typical examples of such methods are short-Time Fourier transform, Wigner–Ville distribution, Wavelet transform, etc. The biggest challenge is achieving optimal time-frequency resolution.

Theoretically, in the time domain the signals can be regarded as having "infinite" time resolution, i.e., one can zoom infinitely many details at an arbitrary time moment, at a cost of having no information about the signal's frequency. The opposite is valid for the pure frequency analysis, where the signal's spectrum contains all the frequency components but is lacking information regarding the time of their occurrence and duration. It should be noted that, by performing digital signal processing, even these methods have limited resolution that is directly connected to the sampling frequency.

Time-frequency analysis methods are bound to a limited time-frequency resolution regardless of the sampling frequency. There is an upper limit for the time-frequency resolution depending on the algorithm and its parameters. Therefore, the main goal is to determine the most suitable signal processing algorithm with such parameters that will result in optimal time-frequency resolution.

2.3.1 Short-Time Fourier Transform

A quite straightforward way of introducing time information bound to a particular spectrum is through the so-called short-time Fourier transform. It is defined as [12]

$$F(\tau, \omega) = \int_{-\infty}^{+\infty} f(t) w(t - \tau) e^{-j\omega t} dt, \tag{2.11}$$

where $w(t)$ is a window function. As such, (2.11) can be regarded as a time localised Fourier transform.

The selection of the window function $w(t)$ is the only parameter. The goal is to have a window function with good time and frequency localisation. The selection of the window and its duration defines the time-frequency resolution of the short-time Fourier transform. The main drawback of the short-time Fourier transform method is that this resolution is fixed.

2.3.2 Wavelet Transform

Wavelet transform resolves the problem of fixed time-frequency resolution by introducing the concepts of scaling a particular waveform with compact support called wavelets. A wavelet function $\psi(t)$ can be scaled and translated by introducing two parameters s and u as

$$\psi_{u,s}(t) = \frac{1}{\sqrt{s}} \psi \left(\frac{t - u}{s} \right). \tag{2.12}$$

CWT of a square integrable function $f(t) \in \mathbf{L}^2(\mathbb{R})$ is defined as [12]

$$Wf(s,u) = \int_{-\infty}^{\infty} f(t)\psi_{u,s}^*(t)\,dt, \tag{2.13}$$

where $\psi_{u,s}(t)$ is defined by (2.12).

Similarly, like the short-time Fourier transform, CWT also offers a way of time-frequency analysis but with adjustable time-frequency resolution. The wavelet coefficients (2.13) depend on the time and frequency characteristics of the function $f(t)$ in the region where the energy of the mother wavelet $\psi_{u,s}(t)$ is concentrated. This region can be described as a rectangle with fixed area, with size scaled with $1/s$.

Strictly speaking, the CWT transform (2.13) describes the analysed signal $f(t)$ on the time-scale plane. The conversion between scale s and actual frequency f is straightforward and depends on the selection of the mother wavelet, the only design parameter in this approach. Each scaling s alters the time-frequency resolution of the mother wavelet. High frequency resolution is preserved for lower frequencies, whereas high time resolution is preserved for higher frequencies.

2.3.3 The Morlet Wavelet

Similarly, like the selection of the window function for the short-time Fourier transform, the selection of the mother wavelet $\psi(t)$ significantly affects the performance of the CWT for the task at hand. In the context of EIS, both amplitude and phase are required. Therefore, the suitable mother wavelet should belong to the family of complex wavelets. Among several choices, two mother wavelets stand out: the Morlet wavelet and the Lognormal wavelet. Generally, it is regarded that the Morlet wavelet offers the optimal time-scale (frequency) resolution [13].

The Morlet wavelet is defined as [14]

$$\psi(t) = \pi^{-\frac{1}{4}} \left(e^{-j\omega_0 t} - e^{-\frac{\omega_0^2}{2}} \right) e^{-\frac{t^2}{2}}, \tag{2.14}$$

where ω_0 is referred to as the wavelet's central frequency and is usually set to a value so that the ratio of the highest two peaks of the wavelet is approximately $\frac{1}{2}$:

$$\omega_0 = \pi \left(\frac{2}{\ln 2} \right)^{\frac{1}{2}} \approx 5.336. \tag{2.15}$$

For $\omega_0 > 5$, the second term in (2.14) can be neglected. The shape of the Morlet wavelet (2.14) is shown in Fig. 2.3.

The Morlet wavelet (2.14) is an analytical function, i.e., it has only positive frequencies. Consequently, the wavelet coefficients $Wf(s,u)$ in (2.13) are complex

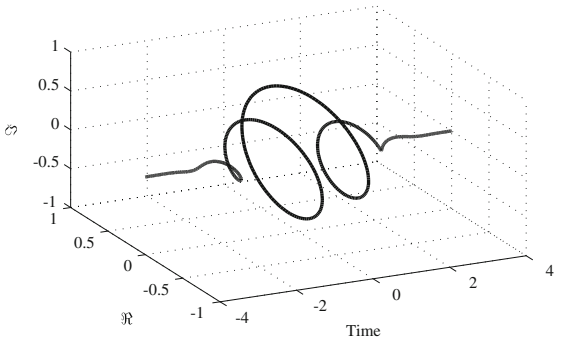

Fig. 2.3 The complex Morlet wavelet

values. As a result, at each time translation u and scale s, the CWT with Morlet wavelet gives the instantaneous amplitude and phase of the analysed signal.

Scale to Frequency Transform for the Morlet Wavelet

The frequencies in CWT (2.13) are represented by scale s, which corresponds to a particular dilatation of the mother wavelet $\psi(t)$. Transforming scale to frequency for the Morlet wavelet is defined as [15]

$$\frac{1}{f} = \frac{4\pi s}{\omega_0 + \sqrt{2 + \omega_0^2}}. \tag{2.16}$$

2.3.4 *Cone of Influence*

The definition of CWT, given by (2.13), specifies infinite length signals. However, the measured signals always have a finite length. The discontinuities (abrupt changes) at the beginning and the end of the observation window influence the wavelet coefficients in their vicinity. Due to the compact support of the mother wavelets, the distortions influenced by these artificial discontinuities affect only a limited number of wavelet coefficients. The affected wavelet coefficients are located in the so-called *cone of influence* that depends on the selected mother wavelet.

These inaccuracies depend on the part of the mother wavelet support that lies outside of the observation time interval as shown in Fig. 2.4. The hatched areas represent the parts of the wavelet support that span outside of the observation window. It has to be noticed that such areas exist on both sides i.e., at the beginning as well as at the end of the observation window. As the mother wavelet is re-scaled for each analysed frequency, the length of these areas varies. Therefore, only not significantly affected wavelet coefficients should be taken into account for any further analysis.

There is a general rule for selecting the unaffected wavelet coefficients, defined as the e-folding time for the autocorrelation of wavelet power at each scale [15]. This value for the Morlet wavelet reads as

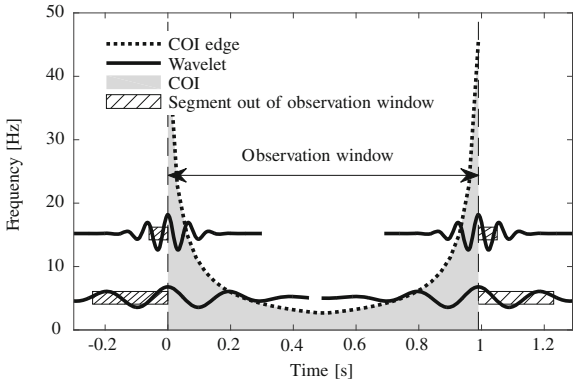

Fig. 2.4 Cone of influence

$$e = s\sqrt{2}. \tag{2.17}$$

The boundary value defined by (2.17) is depicted by the dashed line in Fig. 2.4. The grey area below this boundary line is the cone of influence. The naming *cone* refers to the shape of influenced area's edge over all observed scales. From the shape of the shaded area in Fig. 2.4, it can be noticed that all of the low frequency wavelet coefficients are influenced by the discontinuities occurring on both edges. This in essence means that there are no relevant data for these frequencies. One can overcome this limitation by either using a longer signal or by increasing the sampling frequency of the existing one.

2.3.5 Computationally Efficient CWT with the Morlet Wavelet

The Morlet wavelet allows a computationally efficient implementation of the wavelet transform (2.13). By substituting the mother wavelet $\psi(t)$ with

$$\tilde{\psi}_s(t) = \frac{1}{\sqrt{s}}\psi^*\left(-\frac{t}{s}\right), \tag{2.18}$$

the relation (2.13) transforms into the following convolution:

$$Wf(u,s) = \frac{1}{\sqrt{s}}\int_{-\infty}^{\infty} f(t)\tilde{\psi}_s(u-t)\,dt. \tag{2.19}$$

In the Fourier domain, the convolution (2.19) becomes

$$Wf(u,s) = \frac{1}{2\pi}\int_{-\infty}^{\infty} \hat{f}(\omega)\sqrt{s}\hat{\psi}(s\omega)e^{j\omega u}d\omega, \tag{2.20}$$

where $\hat{f}(\omega)$ is the Fourier transform of the original signal $f(t)$ and $\hat{\psi}(\omega)$ is the Fourier transform of the Morlet wavelet (2.14) [14]:

$$\hat{\psi}(\omega) = \pi^{-\frac{1}{4}} \left(e^{-\frac{(\omega-\omega_0)^2}{2}} - e^{-\frac{\omega^2}{2}} e^{-\frac{\omega_0^2}{2}} \right). \tag{2.21}$$

Therefore, the most computationally demanding process is performed by a simple multiplication in the frequency domain. As a result, the algorithm complexity is governed by the implementation of the FFT algorithm, which has a complexity of $\mathcal{O}(n \log n)$, where n is the number of samples in the signal.

2.3.6 The Lognormal Wavelet

Under certain conditions, the Lognormal wavelet outperforms the Morlet wavelet in terms of time-frequency resolution [11]. The Lognormal wavelet is inline with the logarithmic frequency resolution of the CWT, as it has $\log \omega$ as an argument [11]. The Lognormal wavelet is defined as

$$\hat{\psi}(\omega) = e^{-(\omega_0 \log \omega)^2/2}, \text{ where } \omega > 0. \tag{2.22}$$

The parameter ω_0 can be regarded as the "central frequency" with similar properties as the one of the Morlet wavelet presented in Sect. 2.5. The shape of the lognormal wavelet is shown in Fig. 2.5.

Similarly, as with the Morlet wavelet, the lognormal wavelet allows computationally efficient implementation of the CWT using the same process of calculating the convolution in the frequency domain through FFT. The majority of the results in this book are calculated using the Morlet wavelet unless specified otherwise.

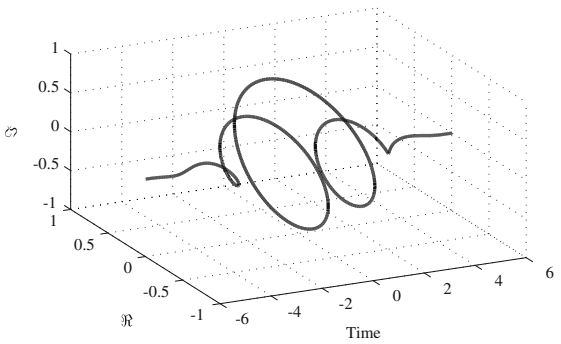

Fig. 2.5 The lognormal wavelet

2.4 Impedance Through Complex Wavelet Coefficients

The result of the CWT analysis of the voltage $u(t)$ and current $i(t)$, with the Morlet wavelet, is a set of complex wavelet coefficients:

$$\begin{aligned} Wi(t, f) &= \Re\{Wi(t, f)\} + j\Im\{Wi(t, f)\}, \\ Wu(t, f) &= \Re\{Wu(t, f)\} + j\Im\{Wu(t, f)\}. \end{aligned} \tag{2.23}$$

Taking into consideration the cone of influence (2.17) and the linearity of the wavelet transform, the impedance can be calculated, similarly as in the case of Fourier transform (2.10), as the following ratio:

$$Z(t, f) = \frac{Wu(t, f)}{Wi(t, f)}. \tag{2.24}$$

The ratio (2.24) provides the value for both the phase and the impedance amplitude in every time-frequency pair. Therefore, by fixing the frequency as $f = f_0$, one is able to estimate the mean impedance value, which is the same as with the calculation through the FFT approach (2.10). However, having the complete time evolution of the complex impedance in every time instance t, one can perform more detailed analysis on the impedance values, for instance estimating the confidence intervals.

2.5 Parameter Selection

For optimal exploitation of the fast EIS method, two parameters have to be specified: (i) the bandwidth of the DRBS excitation f_B and (ii) the central frequency ω_0 of the Morlet mother wavelet. These two parameters influence the sensitivity of the approach with respect to the analysed frequency band, hence their importance for accurate impedance measurements. The parameter selection can be performed in a systematic manner thus guaranteeing optimal performance of the fast EIS approach.

2.5.1 Selection of the DRBS Bandwidth

The rationale behind the selection of the bandwidth parameter f_B is quite intuitive. As shown in Fig. 2.1, the parameter f_B defines the frequency band of the DRBS signal where its frequency spectrum can be considered as sufficiently close to the theoretical flat spectrum of the Gaussian white noise. Therefore, when performing EIS, the frequency band of interest must be contained in the interval $(0, f_b)$. It should be noted that for low frequencies, the previous condition will be always satisfied, which leads to a wrong conclusion that one should just keep the f_B sufficiently high.

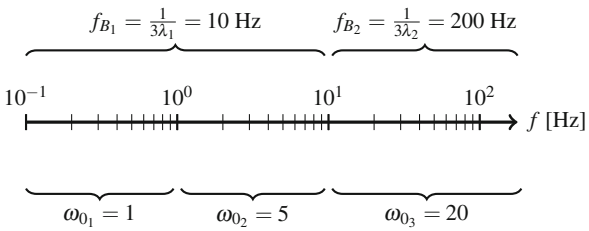

Fig. 2.6 Selection of DRBS bandwidths f_B and Morlet central frequencies ω_0 for a frequency band of interest

Since the energy of the signal is limited, the energy at the individual frequency is proportional to the frequency band f_B. In other words, having high f_B values will cause fast changes in the generated DRBS making it unsuitable for analysing slow responses of the electrochemical system. Therefore, where EIS is performed at low frequencies, the f_B parameter should have low values as well.

From a practical viewpoint, the whole frequency band of interest should be divided into several smaller intervals. The individual bandwith of the employed DRBS excitation should include the maximal frequency of the corresponding interval. One possible way of dividing a frequency band of interest is graphically depicted in Fig. 2.6. The frequency band $[10^{-1}\ 200]$ Hz is divided into two intervals: the low frequency interval, spanning from $[10^{-1}\ 10]$ Hz and the high frequency interval spanning from [10 200] Hz. The corresponding DRBS frequency bands are $f_{B_1} = 10$ Hz and $f_{B_2} = 200$ Hz.

2.5.2 *Influence of the Morlet Wavelet Central Frequency*

The Morlet wavelet central frequency ω_0 determines its time frequency resolution [13, 16]. For smaller ω_0, the shape of the wavelet favours localisation of singular time events, whilst for larger ω_0 more periods of the sine-carrier in the Gaussian window (envelope) make the frequency localisation better.

The broad frequency band and relatively short duration of measured signals raise a problem in relation to the variance of the impedance measurements. The issue is more expressed for lower frequencies. This is due to the fact that at lower frequencies the whole signal contains less periods than the wavelet itself. As a result, there are a lower number of samples that can be employed for estimating the measurement variance. One way of addressing this issue is by lowering the central frequency ω_0.

For the subsequent analysis performed in the following chapters, the observed frequency interval is usually divided into several segments. An example of such a division is presented in Fig. 2.6. Each frequency band is then analysed with the Morlet wavelet whose central frequency is appropriately tuned.

2.6 Accuracy of the Amplitude and Phase Estimates from Wavelet Coefficients

According to the analysis performed by Sejdic et al. [17], estimating the instantaneous amplitude and phase through wavelet coefficients introduces bias. More importantly, the variance and the bias of these estimates depend on the nature of the analysed signal. Due to the discontinuities in the employed DRBS excitation signal, the error in these estimates is further increased.

A simple solution is to make a band-limited version of the DRBS excitation covering only the frequency interval of interest. This can be simply achieved by low-pass filtering the DRBS excitation in such a manner that only the first two lobes of its amplitude spectrum are preserved, i.e., filtering the DRBS signal up to a frequency of $2/\lambda$, as shown in Fig. 2.2.

2.7 Summary

The chapter outlines the fast EIS technique based on discrete random binary sequence excitation and continuous wavelet transform. Unlike the time-averaged impedance values provided by the Fourier transform, the fast EIS technique allows calculation of instantaneous impedance values for an arbitrary set of frequencies. The fast EIS technique is, in the terms of computational complexity, comparable with the Fourier approach. This is achieved by calculating the CWT convolution in the frequency domain.

Optimal impedance results are achieved by using the CWT Morlet mother wavelet. As a result, the fast EIS technique depends on two parameters, the wavelet's central frequency ω_0 and the bandwidth of the excitation signal. The selection of these parameters is straightforward, adding to the applicability of the approach.

Finally, the time-frequency analysis opens the possibility of detailed statistical analysis of the impedance values. Such an analysis is impossible when solely using frequency domain analysis. As it will be shown in the following chapters, the statistical analysis will offer insight on the measurement accuracy as well as open the possibility of using the impedance values for performing various tasks of condition monitoring.

References

1. Yuan, Xiao-Zi, Haijiang Wang, Jian Colin Sun, and Jiujun Zhang. 2007. AC impedance technique in PEM fuel cell diagnosis - a review. *International Journal of Hydrogen Energy* 32: 4365–4380.

2. Wu, Jinfeng, Xiao Zi Yuan, Haijiang Wang, Mauricio Blanco, Jonathan J. Martin, and Jiujun Zhang. 2008. Diagnostic tools in PEM fuel cell research: part I electrochemical techniques. *International Journal of Hydrogen Energy* 33 (6): 1735–1746.
3. Petrone, R., Z. Zheng, D. Hissel, M.C. Péra, C. Pianese, M. Sorrentino, M. Becherif, and N. Yousfi-Steiner. 2013. A review on model-based diagnosis methodologies for PEMFCs. *International Journal of Hydrogen Energy* 38 (17): 7077–7091. doi:10.1016/j.ijhydene.2013.03.106.
4. Zheng, Z., R. Petrone, M.C. Péra, D. Hissel, M. Becherif, C. Pianese, N. Yousfi-Steiner, and M. Sorrentino. 2013. A review on non-model based diagnosis methodologies for PEM fuel cell stacks and systems. *International Journal of Hydrogen Energy* 38 (21): 8914–8926. doi:10.1016/j.ijhydene.2013.04.007.
5. Niya, Seyed Mohammad Rezaei, and Mina Hoorfar. 2013. Study of proton exchange membrane fuel cells using electrochemical impedance spectroscopy technique - a review. *Journal of Power Sources* 240: 281–293. doi:10.1016/j.jpowsour.2013.04.011.
6. Lasia, Andrzej. 2014. *Electrochemical impedance spectroscopy and its applications*. New York: Springer. doi:10.1007/978-1-4614-8933-7.
7. Yuan, Xiao-Zi, Chaojie Sons, Haijiang Wang, and Jiujun Zhang. 2010. *Electrochemical impedance spectroscopy in PEM fuel cells, fundamentals and applications*. London: Springer.
8. Isermann, Rolf, and Marco Münchhof. 2011. *Identification of dynamic systems: an introduction with applications*. Advanced textbooks in control and signal processing. Berlin: Springer. doi:10.1007/978-3-540-78879-9.
9. Davies, W.D.T. 1970. *System identification for self-adaptive control*. New York: Wiley.
10. Ljung, Lennart. 1999. *System identification: theory for the user*, 2nd ed. Prentice-Hall information and system sciences series. Upper Saddle River: Prentice-Hall.
11. Iatsenko, Dmytro. 2015. *Nonlinear mode decomposition*. Springer theses. Springer International Publishing.
12. Mallat, Stéphane. 2008. *A wavelet tour of signal processing: the sparse way*, 3rd ed. Amsterdam: Elsevier Academic Press.
13. Stefanovska, Aneta, and Maja Bračič. 1999. Physics of the human cardiovascular system. *Contemporary Physics* 40 (1): 31–55.
14. Daubechies, Ingrid. 1992. *Ten lectures on wavelets*. CBMS-NSF regional conference series in applied mathematics. Philadelphia: Society for Industrial and Applied Mathematics.
15. Torrence, Christopher, and Gilbert P. Compo. 1998. A practical guide to wavelet analysis. *Bulletin of the American Meteorological Society* 79: 61–78.
16. Musizza, Bojan, Aneta Stefanovska, Peter V.E. McClintock, Milan Paluš, Janko Petrovčič, Samo Ribarič, and Fajko F. Bajrović. 2007. Interactions between cardiac, respiratory and EEG-δ oscillations in rats during anaesthesia. *The Journal of Physiology* 580 (1): 315–326. doi:10.1113/jphysiol.2006.126748.
17. Sejdic, E., I. Djurovic, and L. Stankovic. 2008. Quantitative performance analysis of scalogram as instantaneous frequency estimator. *IEEE Transactions on Signal Processing* 56 (8): 3837–3845. doi:10.1109/TSP.2008.924856.

Chapter 3
Statistical Properties

Due to the nature of the DRBS excitation signal and the Morlet mother wavelet, the resulting impedance values can be treated as complex random variables. This chapter addresses the issue of specifying the complete statistical properties of impedance components at a particular frequency. It exploits the fact that the calculated wavelet coefficients are complex Gaussian circular random variables [1]. As a result, the impedance values are a ratio of two dependent circular complex Gaussian random variables. The following sections present a complete derivation of the corresponding PDFs and cumulative distribution functions (CDFs) of the impedance real and imaginary components as well as its module.

3.1 The Concept of Complex Circular Random Variable

A Gaussian complex random variable can be analysed through its real and imaginary components

$$C = A + jB, \tag{3.1}$$

where both A and B are independent real Gaussian random variables. In order for the complex Gaussian random variable C to be circular, the following condition has to be fulfilled [2]:

$$E[C^2] = E[A^2] - E[B^2] + jE[AB] = 0. \tag{3.2}$$

If A and B are Gaussian random variables, fulfilling (3.2) implies the following:

$$\begin{aligned} E[A^2] &= E[B^2] \\ E[AB] &= 0. \end{aligned} \tag{3.3}$$

P. Boškoski et al., *Fast Electrochemical Impedance Spectroscopy*,
SpringerBriefs in Applied Sciences and Technology,
DOI 10.1007/978-3-319-53390-2_3

The relations (3.3) state that the Gaussian random variables A and B are independent with same variance.

3.1.1 Circularity of Spectral Components

The spectral components of stationary random signals are also complex circular random variables. This can be easily shown by representing a stationary random signal using the Cramer representation [1]:

$$x(t) = \int_{-\infty}^{\infty} e^{j\omega t} dX(\omega), \tag{3.4}$$

where $dX(\omega)$ are complex random variables directly related to the signal's power spectrum. The random variables $dX(\omega)$ have the following properties:

$$E[dX(\omega)] = 0, \;\; E[dX(\omega_1)dX(\omega_2)] = 0, \;\text{for}\; \omega_1 \neq \omega_2. \tag{3.5}$$

Following the definition of circularity defined by (3.3), the relation (3.5) shows that the spectral components $dX(\omega)$ of the stationary random signals are circular complex random variables [2].

This property becomes even more evident by directly exploiting the stationary property of the signal (3.4). The PDF of both $x(t)$ and time translated version $x(t + \Delta t)$ are the same. Following the time translation theorem of the Fourier transform, the Cramer representation of the translated version has spectral components located at $dX(\omega)e^{-j\omega\Delta t}$, yet still having the same PDF as the original $dX(\omega)$. This shows that the PDF of the complex spectral components of a stationary random signal are rotation invariant, i.e., these random variables are complex circular ones.

3.1.2 Circularity of DRBS Spectral Components

Being a stationary random signal, the frequency components of DRBS are circular complex Gaussian random variables. This is graphically shown in Fig. 3.1. Figure 3.1a shows the DRBS signal in the time domain with arbitrary units. The complex CWT coefficients of the DRBS signal for a single frequency are shown in Fig. 3.1b. It is obvious that the resulting distribution is rotation invariant, hence the complex circularity of the spectral component. This is further supported by the histograms of the real and imaginary components of the wavelet coefficients shown in Fig. 3.1c and d, respectively. Both components are distributed according to the Gaussian distribution with zero-mean and same variance.

As noted in Sect. 2.1, DRBS is often implemented as PRBS. For the performed statistical analyses to be valid, the observation window must be longer than the period

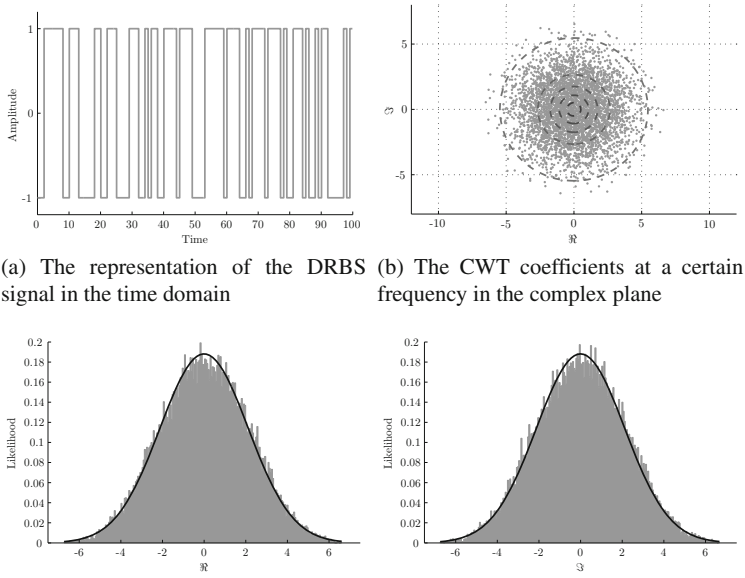

(a) The representation of the DRBS signal in the time domain

(b) The CWT coefficients at a certain frequency in the complex plane

(c) Histogram of the CWT coefficients' real part values and the maximum likelihood estimate of the distribution

(d) Histogram of the CWT coefficients' imaginary values and the maximum likelihood estimate of the distribution

Fig. 3.1 Graphical presentation of the complex Gaussian circularity of DRBS' frequency components

of the PRBS excitation. Furthermore, by using only the low frequency part of the PRBS signal ($f \leq \frac{1}{3\lambda}$), the excitation can be treated as a stationary random one [3].

3.2 Statistical Properties of Measured Impedance

According to (2.10), the impedance of an electrochemical device is a complex variable that is defined as a frequency domain ratio of the voltage to the current. By considering an electrochemical device as a linear and time invariant system, the electrical impedance can be referred as its transfer function, which has a deterministic nature for each frequency.

Following the procedure described in Chap. 2, the impedance characteristic can be efficiently measured by using the CWT complex wavelet coefficients of the electrochemical device's current $i(t)$ and voltage $u(t)$ using the Morlet mother wavelet. Analysing the DRBS signal with CWT preserves its statistical properties within the wavelet coefficients (2.23). Consequently, the wavelet coefficients for a particular frequency can be regarded as a zero-mean Gaussian circular complex random variable [2] with the following properties:

$$\begin{aligned}\Re\{Wi(t,f)\}, \Im\{Wi(t,f)\} &\sim \mathcal{N}\left(0, \frac{\sigma_i^2}{2}\right), \\ \Re\{Wu(t,f)\}, \Im\{Wu(t,f)\} &\sim \mathcal{N}\left(0, \frac{\sigma_u^2}{2}\right),\end{aligned} \tag{3.6}$$

where the corresponding variances σ_u^2 and σ_i^2 are parameters that should be estimated.

3.2.1 Probability Distribution of the Measured Impedance

According to (3.6), the wavelet coefficients $Wi(t,f)$ and $Wu(t,f)$ at a particular frequency $f = f_0$ are Gaussian complex circular random variables. Therefore, the impedance $Z(t,f_0)$ defined by (2.24) is a ratio of two complex random variables. The PDF of the ratio of two random variables can be derived by defining two transformations, such as

$$Z = \frac{U}{I} \quad Y = I. \tag{3.7}$$

Therefore, the joint PDF $f_{Z,Y}(z,y)$ can be obtained through the joint PDF of the original two variables $f_{U,I}(u,i)$ as

$$f_{Z,Y} = |J| f_{U,I}\left(h_1(z,y), h_2(z,y)\right), \tag{3.8}$$

where

$$h_1(z,y) = zy \quad h_2(z,y) = y \tag{3.9}$$

and $|J|$ is the Jacobian determinant as

$$|J| = \begin{vmatrix} \frac{\partial h_1(z,y)}{\partial z} & \frac{\partial h_1(z,y)}{\partial y} \\ \frac{\partial h_2(z,y)}{\partial z} & \frac{\partial h_2(z,y)}{\partial y} \end{vmatrix} = |y|. \tag{3.10}$$

Therefore, the PDF of the ratio can be obtained by integrating out the dummy variable y from (3.8) as

$$f_Z(z) = \int_{-\infty}^{\infty} |J| f_{U,I}\left(h_1(z,y), h_2(z,y)\right) dy = \int_{-\infty}^{\infty} |y| f_{U,I}(zy, y) dy. \tag{3.11}$$

In the context of impedance measurement, the variables U and I in (3.8) are the wavelet coefficients $Wu(t,f_0)$ and $Wi(t,f_0)$, respectively. Using the wavelet coefficients, the joint PDF $f_{U,I}(u,i)$ in (3.8) is the bivariate complex Gaussian distribution with the following covariance matrix:

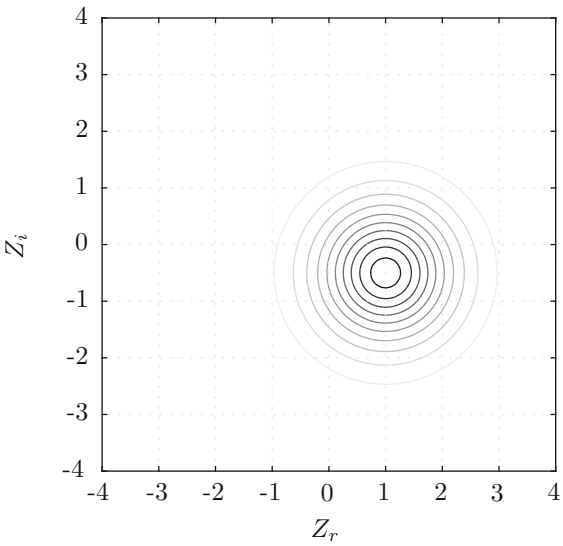

Fig. 3.2 Contour plot of the probability density function (3.13) for $\sigma_u^2 = 4$, $\sigma_i^2 = 1$ and $\rho = \frac{1}{2} + j\frac{1}{4}$

$$\Sigma = \begin{bmatrix} \sigma_u^2 & \rho\sigma_u\sigma_i \\ \rho^*\sigma_u\sigma_i & \sigma_i^2 \end{bmatrix}, \tag{3.12}$$

where $\rho = \rho_r + j\rho_i$ is the complex correlation coefficient, where $|\rho| \leq 1$. Under these conditions, the integral from (3.11) has a close form solution as [4]

$$f_Z(z) = \frac{1 - |\rho|^2}{\pi\sigma_u^2\sigma_i^2}\left(\frac{|z|^2}{\sigma_u^2} + \frac{1}{\sigma_i^2} - 2\frac{\rho_r z_r - \rho_i z_i}{\sigma_u\sigma_i}\right)^{-2}, \tag{3.13}$$

where z_r and z_i are real and imaginary components of the random variable Z. The location of the mode of $f_Z(z)$ depends on the correlation coefficient ρ. The shape of (3.13) is shown in Fig. 3.2.

3.2.2 *Probability Distribution of Impedance Components*

The PDFs of the real z_r and imaginary z_i components of the impedance can be derived from the PDF (3.13). The PDF of the imaginary component z_i reads [4]

$$f_{z_i}(z_i|\rho_r, \rho_i) = \frac{\left(1 - |\rho|^2\right)\sigma_x^2\sigma_y}{2\left(\left(1 - \rho_r^2\right)\sigma_x^2 + 2z_i\rho_i\sigma_x\sigma_y + z_i^2\sigma_y^2\right)^{3/2}}. \tag{3.14}$$

For the real component z_r the PDF has the same shape and reads

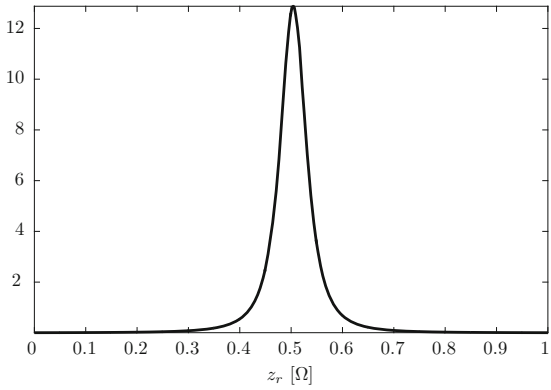

(a) PDF of z_r (3.15)

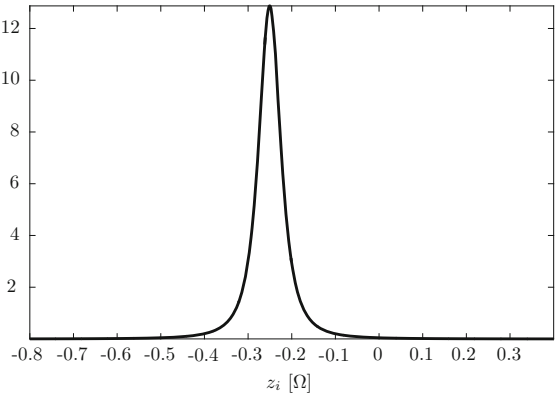

(b) PDF of z_i (3.14)

Fig. 3.3 Examples of PDFs of particular impedance components

$$f_{z_r}(z_r|\rho_r, \rho_i) = f_{z_i}(z_r| - \rho_i, -\rho_r). \tag{3.15}$$

The shape of the (3.14) and (3.15) are shown in Fig. 3.3a and b.

According to Baxley et al. [4], integrating out z_r from (3.13) results in the following CDF:

$$F_{z_i}(z_i|\rho_r, \rho_r) = \frac{1}{2} + \frac{\rho_i\sigma_u + z_i\sigma_i}{2\sqrt{\left(1-\rho_r^2\right)\sigma_u^2 + 2z_i\rho_i\sigma_u\sigma_i + z_i^2\sigma_i^2}}. \tag{3.16}$$

3.2.3 Probability Distribution of the Impedance Amplitude

For the circular Gaussian complex random variables (3.6), their corresponding modules $|Wu(t, f_0)|$ and $|Wi(t, f_0)|$ are distributed with Rayleigh distribution as

$$\begin{aligned} |Wu(t, f_0)| &\sim \text{Rayleigh}(\sigma_u) \\ |Wi(t, f_0)| &\sim \text{Rayleigh}(\sigma_i). \end{aligned} \tag{3.17}$$

As the current $i(t)$ and voltage $u(t)$ are correlated, the PDF of the module of the ratio (2.24) reads [5]

$$f_{|Z|}(|z|) = \frac{2\sigma_i^2\sigma_u^2(1-\rho^2)|z|(\sigma_i^2|z| + \sigma_u^2)}{\left[(\sigma_i^2|z|^2 + \sigma_u^2)^2 - 4\rho^2\sigma_u^2\sigma_i^2|z|^2\right]^{3/2}}, \; |z| \geq 0, \tag{3.18}$$

where $|\rho| \leq 1$ is the correlation coefficient as defined in (3.12). The PDF (3.18) is positively skewed and defined on the non-negative semi axis. A typical realisation of the probability distribution function (3.18) is shown in Fig. 3.4.

The CDF that corresponds to (3.18) reads [5]

$$F_{|Z|}(z) = \frac{1}{2} - \frac{\sigma_u^2 - z^2\sigma_i^2}{2\sqrt{4z^2\left(1-\rho^2\right)\sigma_i^2\sigma_u^2 + \left(\sigma_u^2 - z^2\sigma_i^2\right)^2}}, \tag{3.19}$$

where $z \geq 0$.

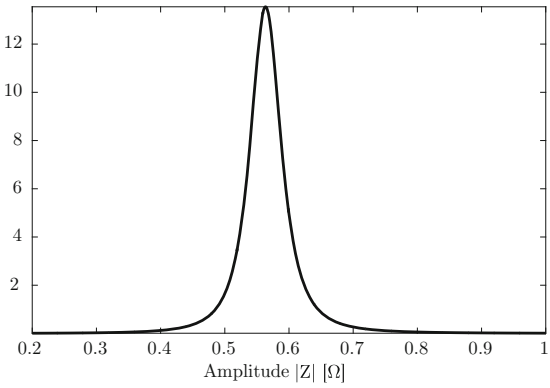

Fig. 3.4 Example of PDF of the module of the impedance (3.18)

3.2.4 Parameter Estimation

The PDF (3.13), (3.14) and (3.18) depend on three parameters σ_u, σ_i, and the correlation coefficient ρ. These parameters can be easily estimated through the covariance matrix (3.12) by using the calculated wavelet coefficients as

$$\begin{aligned} E\{Wu(t,f_0)Wu(t,f_0)^*\} &= \frac{\sigma_u^2}{2} \\ E\{Wi(t,f_0)Wi(t,f_0)^*\} &= \frac{\sigma_i^2}{2} \\ E\{Wi(t,f_0)Wu(t,f_0)^*\} &= \frac{\sigma_u\sigma_i}{2}\rho. \end{aligned} \tag{3.20}$$

3.3 Summary

Having specified the PDFs and CDFs in closed form has specific practical merits. First, one can directly assess the measurement accuracy and correspondingly tune the CWT parameters. Secondly, the maximum likelihood estimation of the PDF parameters exists in closed form, which significantly reduces the computational load of the whole process. The results presented in this chapter will serve as the base in the development of an optimal condition monitoring system.

References

1. Priestley, M.B. 1981. *Spectral analyses and time series*. London: Academic Press.
2. Amblard, P.O., M. Gaeta, and J.L. Lacoume. 1996. Statistics for complex variables and signals - Part I: Variables. *Signal Processing* 53: 1–13.
3. Doebelin, Ernest O. 1980. *System modeling and response*. New Jersey: Wiley.
4. Baxley, R.J., B.T. Walkenhorst, and G. Acosta-Marum. 2010. Complex Gaussian ratio distribution with applications for error rate calculation in fading channels with imperfect CSI. In *IEEE GLOBECOM 2010*.
5. Simon, Marvin, K. 2006. *Probability distributions involving gaussian random variables*. Heidelberg: Springer Science.

Chapter 4
Test Cases

The fast EIS technique, presented in Chap. 2, is applicable to all types of electrochemical devices and beyond. The goal of this chapter is to demonstrate the applicability and effectiveness of the fast EIS by means of both simulations and in-the-field measurements. Therefore, this chapter includes impedance measurement results performed by the fast EIS technique on the following types of devices:

- RC circuits,
- an industrial PEM fuel cell system,
- a Li-ion battery, and
- a laboratory-grade Li-S cell.

4.1 RC Circuits

RC circuits offer a straightforward way for validating impedance measurement techniques. Generally, an RC circuit can be regarded as a truly linear and time-invariant system. Furthermore, the impedance of such a circuit is simple and can be derived in a closed form. Therefore, the applicability of the fast EIS technique can be validated both on simulated as well as on real RC circuits. For that purpose, two different RC circuits are used:

1. a simple first-order RC circuit (low pass filter with cutoff frequency at approximately 1.6 kHz), and
2. a second-order cascaded RC circuit (with impedance characteristic similar to that of a PEM fuel cell).

The simulated results for the RC circuits are obtained using noise-free signals. Afterwards, the same procedure is repeated for real implementation of those two RC circuits with real signals (with noise present).

P. Boškoski et al., *Fast Electrochemical Impedance Spectroscopy*,
SpringerBriefs in Applied Sciences and Technology,
DOI 10.1007/978-3-319-53390-2_4

4.1.1 Measurement Equipment

A custom made electronics circuit was built for performing impedance measurements on low-power devices, which was used with the RC circuits and Li-S cells. The electronics consists of a bidirectional current source (i.e., source and load) and signal condition circuitry. The bidirectional source provides small-amplitude current signal excitation superimposed on top of a DC component. At the same time, the signal conditioning part of the circuit filters and amplifies all the relevant AC signals allowing very accurate measurements over a wide frequency range.

The block diagram of the circuit is shown in Fig. 4.1. The current through the device under test is controlled over two inputs. The *DC current reference* input is used to control the DC component of the current and the *AC current excitation reference* input is used for imposing the excitation waveform. A shunt resistor is used for measuring the electrical current that passes through the tested device. Only the AC components of the current and voltage signals are relevant for EIS. Therefore, the signals are first high-pass filtered and then amplified in order to achieve high resolution. Additionally, the circuit provides low-pass filtered outputs for monitoring the DC component of the signals. All the signals are fed to a data acquisition device (e.g., National Instruments USB DAQ module) for A/D conversion.

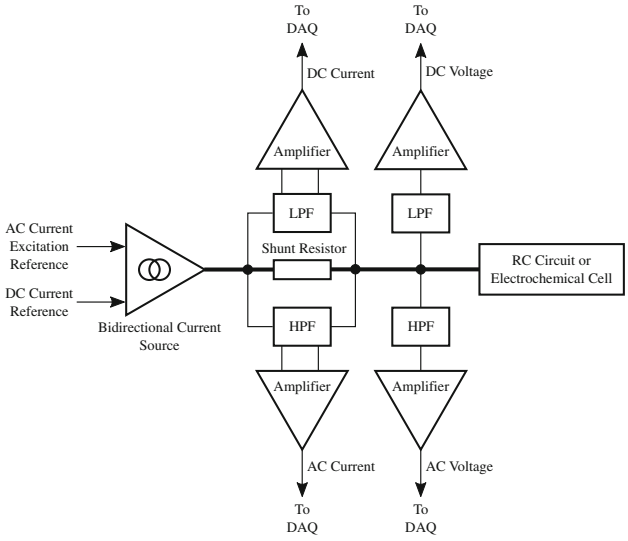

Fig. 4.1 Block diagram of the electronics circuit for performing impedance measurements on low-power devices (LPF – low pass filter, HPF – high pass filter)

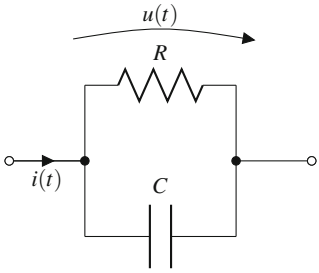

Fig. 4.2 First-order RC circuit

4.1.2 First-Order RC Circuit

A first-order RC circuit is the simplest form of an RC circuit. Such a circuit consists of a single resistor R and a capacitor C connected in parallel as shown in Fig. 4.2. In the complex domain, its impedance reads as follows:

$$Z(j\omega) = \frac{R}{1 + j\omega RC}. \tag{4.1}$$

The parameters of the tested first-order RC circuit are $R = 500.2\,\Omega$ and $C = 202.38\,\text{nF}$. The resistance R and capacitance C values determine the time constant τ of the circuit,

$$\tau = RC = 101.2\ \mu\text{s}, \tag{4.2}$$

and the corresponding cutoff frequency f_{cutoff},

$$f_{cutoff} = \frac{1}{2\pi\tau} = 1572\ \text{Hz}. \tag{4.3}$$

The theoretical impedance characteristic is shown in Fig. 4.3.

Simulation

The simulation is performed in three steps. First, the DRBS excitation signal is generated using the Octave/Matlab script given in Listing A.1. Secondly, the generated excitation signal is used as an input for simulation of an RC circuit system with transfer function given with (4.1). The simulation is given in Listing A.2. Finally, the impedance characteristic is computed by employing CWT using the code presented in Listing A.3. All other depending scripts are listed in Appendix A.

The comparison between the theoretical impedance characteristic of the RC circuit and the one computed through fast EIS is presented in Fig. 4.3. The impedance is computed at 20 points in the frequency interval from 15 Hz to 15 kHz. At each frequency the contour plot depicts the shape of the complex distribution (3.13). As expected, the values of the theoretical impedance coincide with the mean value of the complex distribution at the corresponding frequency. The simulation results are

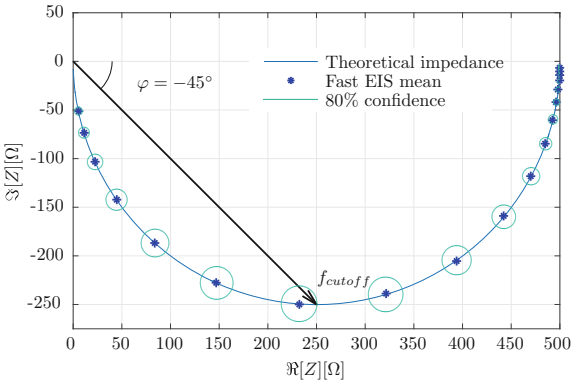

Fig. 4.3 Theoretic impedance characteristic of the first-order RC circuit and fast EIS impedance measurements ($R = 500.2\,\Omega$ and $C = 202.38\,\text{nF}$)

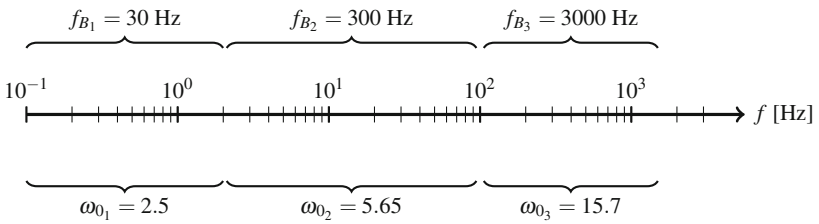

Fig. 4.4 Partition of the frequency band for impedance measurement of the cascade RC circuit

obtained with signals without any additive noise. Therefore, only a single DRBS excitation signal is used with sufficiently high bandwidth f_B.

Measurement

The parameters of the real RC circuit are the same as with the simulated one ($R = 500.2\,\Omega$ and $C = 202.38\,\text{nF}$).[1] The measurements were carried out using the electronic circuit described in Sect. 4.1.1. The impedance was measured in the frequency band $f \in [0.2, 1500]\,\text{Hz}$. This frequency band was divided into three segments. For each segment, a different combination of DRBS bandwidth f_B and wavelet central frequency ω_0 was used, as shown in Fig. 4.4. The measurement time for each DRBS excitation was 7.5 s, resulting in 22.5 s required for complete characterisation.

The impedance obtained with the fast EIS technique is shown in Fig. 4.5, where the diamonds represent the computed mean value of the distribution (3.13). As expected, the measured impedance values coincide with the theoretical ones.

[1] In fact, the RC values for the simulation were chosen based on the values of the real resistor and capacitor values used for measurements.

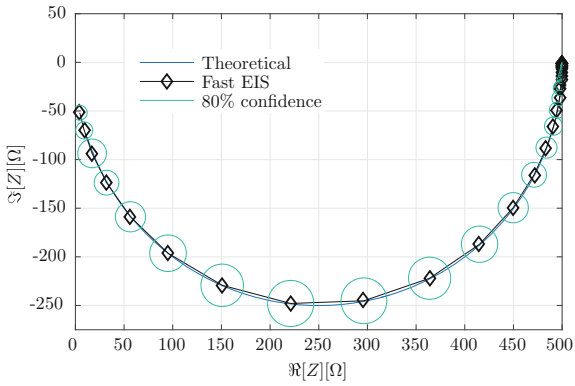

Fig. 4.5 Measured impedance characteristic of the first-order RC circuit

4.1.3 Cascaded RC Circuit

Typically, electrochemical energy systems are modelled with equivalent, high-order circuits that are a combination of first-order RC circuits. The general architecture includes several RC circuits connected in series with additional non-linear components. Following the same idea, a linear, cascaded, second-order *RC* circuit was employed, as shown in Fig. 4.6.

The impedance of the circuit shown in Fig. 4.6 reads

$$Z = \frac{R_1}{1 + j\omega R_1 C_1} + \frac{R_2}{1 + j\omega R_2 C_2}. \tag{4.4}$$

The parameters of the cascaded RC circuit are $R_1 = 500.2\,\Omega$, $C_1 = 202.38\,\text{nF}$, $R_2 = 1000.3\,\Omega$, $C_2 = 4.9645\,\mu\text{F}$.

Simulation

For the simulation of the cascaded RC circuit, the same excitation signals are used as in the case of the first-order RC circuit presented in Sect. 4.1.2. The only difference is in the simulation code, i.e., the Listing A.2 is replaced with the Listing A.4.

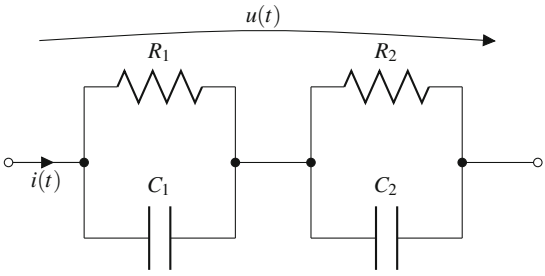

Fig. 4.6 Cascaded second-order RC circuit

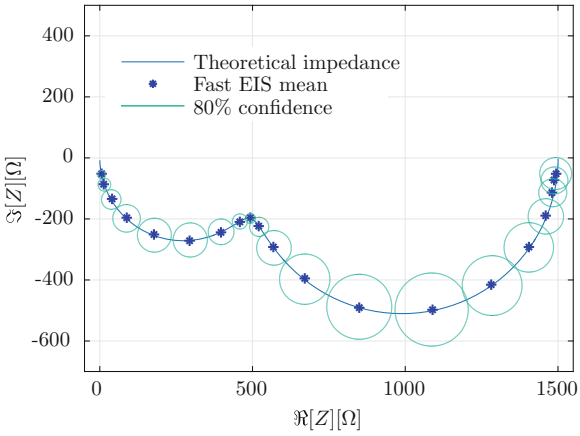

Fig. 4.7 Theoretic impedance characteristic of the cascaded RC circuit and fast EIS impedance measurements ($R_1 = 500.2\,\Omega$, $C_1 = 202.38\,\text{nF}$, $R_2 = 1000.3\,\Omega$, $C_2 = 4.9645\,\mu\text{F}$)

The impedance is computed in the frequency interval from 1.5 Hz to 15 kHz. The measured impedance characteristic is shown in Fig. 4.7. The contour plots depict the 80% confidence interval for each impedance estimate. The confidence intervals were calculated using the corresponding complex probability distribution function (3.13). As the simulations were performed without any noise, similar to the first-order RC circuit, only one DRBS signal was used with sufficiently high bandwidth.

Measurement

The impedance characteristic of the cascaded RC circuit was measured using the same measurement equipment as in the case of single RC circuit (see Sect. 4.1.1). Following the same procedure as in the case of the first-order RC circuit, the same partition of the frequency band $f \in [0, 1500]$ Hz was also used for this circuit (see Fig. 4.4).

The resulting impedance characteristic is shown in Fig. 4.8. The plot includes the measured mean values of the PDF (3.13) and the corresponding confidence intervals at 80%. The changes of the parameters of f_B and ω_0 are clearly visible via changes in the measurement variance. In the lowest frequency band, the variance is sufficiently low. However, it gradually increases as the frequency of the measured impedance becomes closer to the limit frequency f_{B_1}. As the second DRBS is employed, there is a sudden decrease of the measurement variance. The variance of the high frequency semicircle is even smaller predominantly due to two factors. The first factor is the change to f_{B_3} and ω_{0_3}. The second is that, for high frequencies, there are significantly more periods for shorter observation time.

4.2 Li-Ion Battery

The measurements were performed on an industrial grade 20 Ah Li-ion battery with 4 cells connected in series. The approximate terminal voltage of the battery is 12 V. The impedance characteristic was measured in the frequency interval from 0.5 Hz

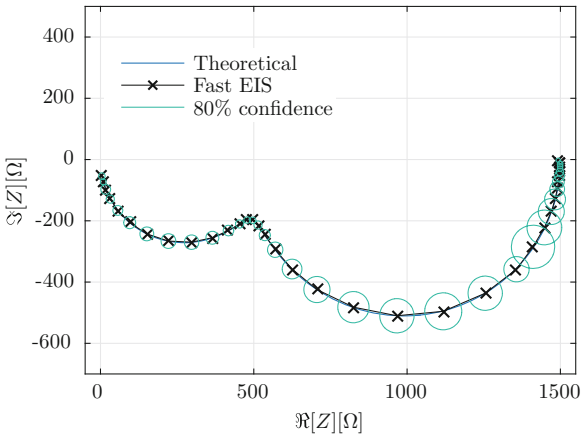

Fig. 4.8 Measured impedance characteristic of the cascaded RC circuit

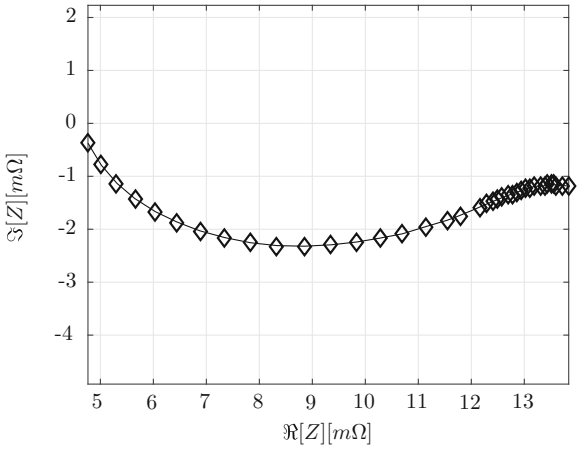

Fig. 4.9 Impedance characteristic of the Li-ion battery

up to 1.5 kHz. The measurements were performed using an Amrel PLW9K-120 electronic load and general purpose data acquisition module. The electronic load provided the DRBS excitation required for the fast EIS technique. The estimated battery impedance characteristic is shown in Fig. 4.9.

The impedance characteristics shown in Fig. 4.9 exhibit two semicircles, as anticipated for Li-ion batteries [1, 2], where the low-frequency semicircle is much less expressed compared to the high-frequency one [3]. Since the measurements were carried out down to 0.5 Hz, only the start of the low-frequency semicircle is visible.

4.3 Li-S Cell

Due to its high energy density, the Li-S battery technology is considered as a prospective candidate particularly for automotive applications. Since industrial grade Li-S batteries are currently unavailable, the fast EIS technique was applied to a small-capacity laboratory prototype Li-S cell. The used Li-S cell has a capacity of approximately 2 mAh and a nominal voltage of 2.4 V. Due to the low capacity of the used laboratory grade Li-S cells, the induced current perturbation has an amplitude of a few μA. The impedance characteristic of the Li-S cell was measured using the same measurement equipment as in the case of the single RC circuit (see Sect. 4.1.1).

Three DRBS signals were employed. The first one with bandwidth $f_{B_1} = 20\,\text{kHz}$ was applied for 7.5 s. The second one with bandwidth $f_{B_2} = 400\,\text{Hz}$ was applied for 30 s. And the last one with bandwidth $f_{B_3} = 40\,\text{Hz}$ was applied for 120 s. Accordingly, three different wavelet central frequencies ω_0 were used $\omega_0 \in \{1.25, 12, 15\}$. The partitioning is shown in Fig. 4.10. The measured impedance characteristics of the Li-S cell in the frequency interval from 0.0.2 Hz up to 20 kHz is shown in Fig. 4.11.

The impedance characteristics clearly shows both high and low frequency semicircles [4]. The three segments corresponding to the three different DRBS excitation signals become distinct by observing the measurement confidence intervals. As expected, the measurement variance is the biggest for the low frequency part of the impedance (the right semicircle). The second DRBS excitation covers the segment in which the real component of the impedance is in the interval $\Re[Z] \in [120, 200]\,\Omega$.

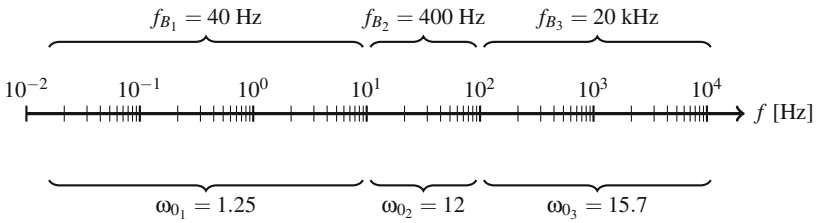

Fig. 4.10 Partition of the frequency band for impedance measurement of the Li-S cell

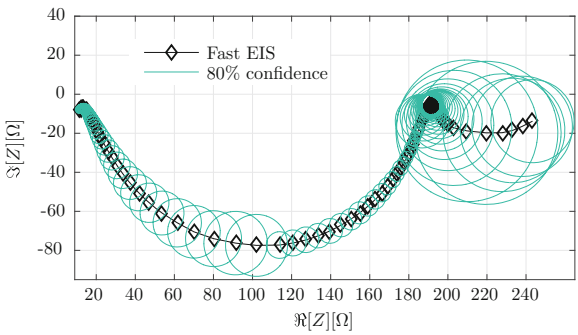

Fig. 4.11 Impedance characteristic of the Li-S cell

The variance gradually increases as the impedance frequency becomes closer to the limit value f_{B_2}. The last segment covers the high frequency values. As a result, the initial measurement variance is high. This is mainly due to the higher wavelet central frequency $\omega_0 = 15\,\text{rad/s}$ used for this frequency interval. The variance is then gradually reduced as the frequency increases.

4.4 PEM Fuel Cells

The impedance measurements on PEM fuel cells were performed using an industrial grade Hydrogenics HyPM-HD 8-200 fuel cell system. During the impedance measurement, the fuel cell was kept at constant operating and environmental conditions. The stack's temperature and the stoichiometry were kept constant by the built-in controller supplied by the fuel cell manufacturer at 50 °C and 2.5, respectively. The fuel cell stack was fed with pure and dry hydrogen at a constant temperature of 20 °C.

The DC current operating point was set to 70 A resulting in the stack voltage of 55 V, whereas the amplitude of the superposed DRBS excitation waveform was set to 2 A. As such, the peak-to-peak amplitude was 4 A and, therefore, small enough in order to preserve the local linear behaviour of the fuel cell. Figure 4.12 shows time plots of current and voltage signals of a PEM fuel cell during measurements. The current was measured as an absolute value, whereas the fuel cell voltage was measured as a differential value.

Two DRBS signals were consecutively applied, one after the other, to the fuel cell system. The first DRBS signal ($f_{B_1} = 166\,\text{Hz}$) was applied for 45 s and the second ($f_{B_2} = 660\,\text{Hz}$) for 15 s; therefore, one individual measurement of impedance characteristic took 60 s. The first DRBS signal was applied for a longer time period since it excites lower frequencies. For comparison, Fouquet et al. [5], who used a conventional single-sine approach, reported that an approximately 5 min long measurement was required to estimate the impedance characteristic, whereas with DRBS

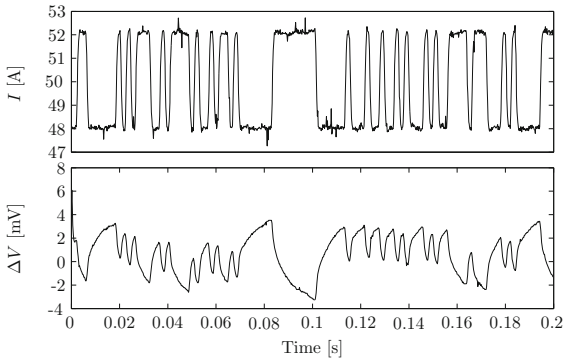

Fig. 4.12 Measured current and voltage signals during the experiment

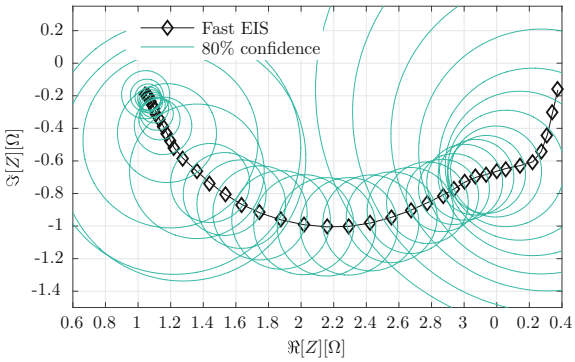

Fig. 4.13 Measured impedance characteristic of the PEM fuel cell

excitation and wavelet transform, the same results are obtained in less than 60 s, in a comparable frequency band.

Figure 4.12 shows an example of the current and voltage signals of a PEM fuel cell during the experiment. It can be noticed that the actual fuel cell current is not of an ideal DRBS waveform. The shape is affected by the presence of the other balance of plant components. The impedance characteristics obtained by the fast EIS technique is presented in Fig. 4.13.

The impedance characteristic in Fig. 4.13 contains the expected two semicircle arcs. The high-frequency arc ranges from approximately 5 Hz up to high frequencies. The low-frequency arc starts at approximately 0.5 Hz and extends up to 5 Hz, where the high-frequency arc starts. The biggest measurement variance is present for the low frequency part. The low frequency part includes slow varying dynamics of the control loops of the tested PEM fuel cell, hence high variance. The influence of the control loops is also visible around 100 Hz (i.e., for impedance values around $1.2\text{-}j0.6\,\Omega$). Outside of this interval the measurement variance decreases as the frequency increases.

4.5 Discussion

The results presented in this section confirm the applicability of the proposed fast EIS technique for various types of electrochemical devices including low-power devices as well as industrial grade Li-ion battery and PEM fuel cells. As shown by the results, there are three main practical benefits of the fast EIS technique:

1. The time required for measuring the complete impedance characteristic is significantly shorter compared to the time required by the conventional (multi-)sine based methods.
2. The impedance characteristic can be calculated at an arbitrary set of frequencies without any impact on the measurement time.
3. Impedance measurements are always accompanied by the measurement variance.

Due to the short measurement time, the fast EIS method is particularly suitable for measuring impedance on batteries during normal operation. While discharging (or charging) a battery breaches the time invariance requirement since its state-of-charge directly influences its impedance characteristic, by having a method that allows for a fast measurement process, one can assume that the changes in the state-of-charge are insignificant thus preserving the important time invariance property.

Due to the broad frequency excitation, the calculation of the impedance can be performed at an arbitrary set of frequencies as long as they are included in the frequency band $f \leq 1/3\lambda$. The calculation process is done offline, i.e., the processing is performed after the data acquisition process has been completed. As a result, the fast EIS technique enables calculation of impedance at an arbitrary frequency resolution. Therefore, the fast EIS technique has a potential for performing online impedance measurements that can be used for continuous monitoring of electrochemical energy systems. The applicability of fast EIS for condition monitoring is covered in the next two chapters of this book.

References

1. Andre, D., M. Meiler, K. Steiner, Ch. Wimmer, T. Soczka-Guth, and D.U. Sauer. 2011. Characterization of high-power lithium-ion batteries by electrochemical impedance spectroscopy. I. Experimental investigation. *Journal of Power Sources* 196 (12): 5334–5341. doi:10.1016/j.jpowsour.2010.12.102.
2. Andre, D., M. Meiler, K. Steiner, H. Walz, T. Soczka-Guth, and D.U. Sauer. 2011. Characterization of high-power lithium-ion batteries by electrochemical impedance spectroscopy. II. Modelling. *Journal of Power Sources* 196 (12): 5349–5356. doi:10.1016/j.jpowsour.2010.07.071.
3. Schmidt, Jan Philipp, Thorsten Chrobak, Moses Ender, Jörg Illig, Dino Klotz, and Ellen Ivers-Tiffée. 2011. Studies on $LiFePO_4$ as cathode material using impedance spectroscopy. *Journal of Power Sources* 196 (12): 5342–5348.
4. Deng, Zhaofeng, Zhian Zhang, Yanqing Lai, Jin Liu, Jie Li, and Yexiang Liu. 2013. Electrochemical impedance spectroscopy study of a lithium/sulfur battery: Modeling and analysis of capacity fading. *Journal of The Electrochemical Society* 160 (4): A553–A558. doi:10.1149/2.026304jes.
5. Fouquet, N., C. Doulet, C. Nouillant, G. Dauphin-Tanguy, and B. Ould-Bouamama. 2005. Model based PEM fuel cell state-of-health monitoring via AC impedance measurements. *Journal of Power Sources* 159: 905–913.

Chapter 5
Statistical Condition Monitoring Tool

The effectiveness of a condition monitoring (CM) system depends on two main characteristics:

1. high diagnostic sensitivity while at the same time retaining sufficient diagnostic stability, and
2. simplified presentation of the diagnostic results in a form understandable by the operator and/or high-level control system.

The crucial parameters for the effectiveness of a CM system are the threshold values that define when a specific alarm is to be raised. Usually, the specification of the threshold values is performed during the commissioning phase of a new system or tuned after a maintenance activity. Improperly tuned threshold values may result either in an excessive number of false alarms, or in a reduced sensitivity of the CM system to deviant conditions (i.e., faults). From the point of view of the user (or control system), having either too high of an alarm rate or missed alarms reduces the reliability of the CM system. Therefore, a method for tuning the CM system's threshold values is of great practical merit.

The tuning of a CM system is usually performed by characterising the monitored system over various fault modes. However, such an approach usually leads to irreversible damage and is therefore generally inapplicable. Moreover, due to variation in parameters from one electrochemical device to another, there is no straightforward way of transferring a CM system's parameters among devices without conducting a new complete set of characterisation procedures. Therefore, a vital question arises of how to design a condition monitoring system employing measurements conducted solely under fault free (normal) operation.

The second requirement, a simplified presentation of the diagnostic results, is particularly important when dealing with electrochemical devices, since the main source of diagnostic information is impedance values. As impedance is measured at numerous frequencies, the resulting feature set has high cardinality. The biggest

P. Boškoski et al., *Fast Electrochemical Impedance Spectroscopy*,
SpringerBriefs in Applied Sciences and Technology,
DOI 10.1007/978-3-319-53390-2_5

challenge is to aggregate the information from such a feature set into a tractable form. Going one step further, this would mean providing a single, so-called, condition indicator that can sufficiently and accurately describe the overall condition of the monitored system.

This chapter presents solutions for both of the identified issues by exploiting the statistical properties of the measured impedance values as described in Chap. 3. As a result, the boundaries of the fault free region can be determined by specifying the desired false alarm rate, which is intuitive and very well understood even by non-specialists in the area of CM. Addressing the issue of information aggregation, this chapter provides an approach of estimating the multidimensional joint CDF of the measured impedance values through the concept of copula functions. This approach exploits the fact that the impedance components are dependent complex random variables and that marginal distributions of each impedance component is known in closed form. As a result, one is able to construct a multi dimensional copula structure that provides a sufficiently accurate approximation of the actual joint CDF of the complete impedance characteristic. Therefore, the output of such a copula structure is a value in the interval [0, 1] and can be treated as a unit-free overall description of the electrochemical system's condition, i.e., an overall condition indicator.

5.1 Optimal Alarm Thresholds Based on the Probability of False Alarm

Determining proper alarm thresholds is an essential step in designing an effectual CM system. Too high thresholds decrease the sensitivity of the diagnostic system to faults and hence increase the probability of missed alarms. Too low thresholds increase the chances of false alarms, which can easily ruin the credibility of the monitoring system. Instead of using the well established way of explicitly stating the threshold values, the presented approach employs the concept of specifying the permitted probability of false alarm (PFA) [1].

PFA determines the acceptable rate of Type I errors when deciding whether a fault has occurred. In the context of electrochemical devices, this can be done by calculating the probability of observing a particular impedance value. Employing the derived corresponding PDFs and CDFs from Chap. 3, the alarm threshold values can be calculated as

$$\begin{aligned} T_{\downarrow} &= F_Z^{-1}\left(\frac{p_{FA}}{2}\right) = \inf\left\{F_Z(z) \geq \frac{p_{FA}}{2}\right\}, \\ T_{\uparrow} &= F_Z^{-1}\left(1 - \frac{p_{FA}}{2}\right) = \inf\left\{F_Z(z) \geq 1 - \frac{p_{FA}}{2}\right\}, \end{aligned} \tag{5.1}$$

where $F_Z(z)$ is the corresponding CDF. Since the impedance Z is complex, it is generally more intuitive to monitor the real and imaginary parts separately or on some case its modulus. Note that expression $\frac{p_{FA}}{2}$ is used to split the PFA between

both ends of the PDF since the presence of different faults can increase or decrease the value of impedance.

In the case of electrochemical devices, the parameters of the corresponding CDF can be estimated by using data solely from fault free operation through relation (3.20). As a result, the tunning of a CM can be performed in a timely manner without the need for complete characterisation of the electrochemical device over a wide range of fault modes. The only design parameter is an easily interpretable PFA value.

Threshold Values for z_i and z_r

The threshold values for z_i (or z_r) can be calculated by solving the inverse CDF (3.16) at arbitrary PFA $y = PFA$ as

$$z_i = \frac{-2(y-1)y\rho_i\sigma_u\sigma_i}{2(-1+y)y\sigma_i^2} \pm \frac{\sqrt{(1-2y)^2(y-1)y\left(|\rho|^2-1\right)\sigma_u^2\sigma_i^2}}{2(-1+y)y\sigma_i^2}. \tag{5.2}$$

Threshold Values for $|z|$

In a similar approach, by solving the inverse CDF of $|z|$ (3.19) for a specific PFA $y = PFA$, the threshold value reads

$$z = \sigma_u \left(\frac{-1+2y-2y^2+(1-2y)^2\rho^2}{2(-1+y)y\sigma_i^2} \pm \frac{(1-2y)\sqrt{-1+\rho^2}\sqrt{(1-2y)^2\rho^2-1}}{2(-1+y)y\sigma_i^2} \right)^{1/2}. \tag{5.3}$$

This approach was used for calculating the thresholds values in Fig. (6.2) for PFA=10%.

5.2 Single Frequency Based Condition Indicator

Selected threshold values (5.1) can be additionally used for mapping the complex impedance values into a so-called condition indicator (CI). It is an abstract feature defined on the interval $[0, \infty)$ that can be directly related to the condition of a system [1]. For a healthy system, CI should acquire low values, typically CI = 0. As the condition deteriorates, the value of CI should increase in accordance with the severity of the fault(s) present in the system. Using the PFA value, the value of CI are typically scaled in such a way that values close to one should indicate imminent failure. Having such a feature value with a fixed threshold determining imminent failure has two major advantages:

1. It gives a unified and unit-free view of the overall system condition; and
2. its trend can be used for prognostics, i.e., estimation of the remaining useful life.

In the context of electrochemical devices, the presence of fault can either increase or decrease certain impedance components. Therefore, for fault free operation, the value of the CI will be in the middle of the region bounded by thresholds at a certain PFA.

The mapping into the corresponding CI can be easily achieved by using the cumulative distribution functions of either (3.14) or (3.18) for the corresponding impedance components. As a result, the impedance components of the fault free region will acquire values in the vicinity of 1/2. Setting the maximal value for the CI to be the chosen PFA, the final scaling relation reads

$$CI = 2 \times (1 - PFA)^{-1} \left| F(z) - \frac{1}{2} \right|, \tag{5.4}$$

where $F(z)$ is the cumulative distribution function of the corresponding impedance component.

The steps of the proposed method for threshold selection are listed in Algorithm 1. The threshold values have to be separately calculated for each individual electrochemical system. The algorithm has to be performed for each system only once (e.g., when commissioning a new system), under fault-free conditions. The only design parameter is the desired PFA value.

Algorithm 1 Determining threshold values

1: **Apply** DRBS excitation signal.
2: **Measure** voltage $u(t)$ and current $i(t)$ signals under fault-free condition.
3: **Estimate** impedance $z(t)$ using (2.24).
4: **Estimate** covariance Σ using (3.12).
5: **Compute** CM thresholds (5.1) using CDF (3.19) and the desired PFA value.

5.3 Dependence Among Complex Random Variables as a Condition Indicator

Following the procedure described in Sect. 5.2, each frequency at which impedance is measured can be associated with one CI (5.4). This leads into a set of CIs with the same cardinality as the set of frequencies at which the impedance is measured. Such a set of CIs has little practical value. Therefore, the goal is to define an overall CI that will aggregate all of the calculated CIs from each frequency into a single value. A possible solution to this problem can be found by employing the concepts of copula function.

As derived in Sect. 3, the impedance values measured through the fast EIS technique are complex random variables. Furthermore, for different frequencies, the measured impedance values are dependent. The dependence originates directly from the physical characteristics of the electrochemical device. Within the statistical analysis framework, the most informative way of analysing dependent random variables is through their joint CDF (or PDF).

Specifying the joint CDF is a difficult task especially for a large number of dimensions [2], such as with the issue at hand. Copula functions offer a solution to this problem by estimating the joint CDF using the marginal distributions. In the context of fast EIS, the marginal distributions are the CDFs of impedance at the selected frequencies of interest. The multivariate joint CDF, specified in such a way, is capable of describing various types of dependences, including nonlinear ones.

The resulting copula structure will model the dependence among the impedance components under fault-free operation. The output of the multi-dimensional copula structure expresses the probability of observing particular impedance values with respect to the initial fault-free condition. By its very nature, its sensitivity to the changes of the underlying marginal distributions enables the detection of the departure from the fault-free condition region described by the original copula structure.

Copula functions have been successfully applied in various fields [3–10]. To the authors' knowledge, this is the first application of this concept for condition monitoring of electrochemical energy systems.

5.3.1 Basics of Copula Functions

The joint PDF of two continuous random variables X_1 and X_2 is equal to

$$f_{X_1,X_2}(x_1, x_2) = f_{X_2|X_1}(x_2|x_1) f_{X_1}(x_1) = f_{X_1|X_2}(x_1|x_2) f_{X_2}(x_2), \tag{5.5}$$

where $f_{X_1}(x_1)$ and $f_{X_2}(x_2)$ are the marginal PDFs, and $f_{X_1|X_2}(x_1|x_2)$ and $f_{X_2|X_1}(x_2|x_1)$ are the corresponding conditional PDFs. The marginal distributions either are known or can be easily estimated from the available data. On the other hand, when x_1 and x_2 are dependent, the conditional PDFs are generally unknown and are usually difficult to estimate. Consequently, the derivation of the joint PDF is not trivial. An elegant way to connect the marginal PDFs of the random variables with their joint PDF is given through copulas.

For two random variables X_1 and X_2, which are defined on the same probability space, the joint CDF $F_{X_1,X_2}(x_1, x_2)$ defines the probability of events in terms of the simultaneous occurrences of X_1 and X_2. Sklar [11, 12] proved that the joint distribution function $F_{X_1,X_2}(x_1, x_2)$ of two random variables is equal to the copula $C(u, v)$.

Theorem 5.1 (Sklar's theorem) *Let $F_{X_1,X_2}(x_1, x_2)$ be a two-dimensional distribution function with marginal distribution functions $F_{X_1}(x_1)$ and $F_{X_2}(x_2)$. Then a copula*

$C(u, v)$ exists such that for all $x_1, x_2 \in \mathscr{R}^2$,

$$F_{X_1,X_2}(x_1, x_2) = C(u, v), \tag{5.6}$$

where $u = F_{X_1}(x_1)$ and $v = F_{X_2}(x_2)$. Moreover, if $F_{X_1}(x_1)$ and $F_{X_2}(x_2)$ are continuous, then $C(u, v)$ is unique. Otherwise $C(u, v)$ is uniquely determined on the Cartesian product $Im(F_{X_1}) \times Im(F_{X_2})$. Conversely, if $C(u, v)$ is a copula and $F_{X_1}(x_1)$ and $F_{X_2}(x_2)$ are distribution functions then $F_{X_1,X_2}(x_1, x_2)$ is a two–dimensional distribution function with marginals $F_{X_1}(x_1)$ and $F_{X_2}(x_2)$.

A bivariate copula function $C : [0, 1]^2 \rightarrow [0, 1]$ is an aggregation function that satisfies [13]:

1. $C(x, 0) = C(0, x) = 0$ and $C(x, 1) = C(1, x) = x$ for all $x \in [0, 1]$ (boundary conditions);
2. $C(x_1, y_1) - C(x_1, y_2) - C(x_2, y_1) + C(x_2, y_2) \geq 0$, for all $x_1, y_1, x_2, y_2 \in [0, 1]$ such that $x_1 \leq x_2$ and $y_1 \leq y_2$ (2-increasing property).

According to Sklar's theorem [12, 13], there exists a multivariate CDF $C_\theta(u, v)$, where θ is a parameter that has to be estimated, and u and v are uniformly distributed random variables on the unit interval [0, 1]. Therefore, the joint CDF $F_{X_1,X_2}(x_1, x_2)$ reads as follows:

$$F_{X_1,X_2}(x_1, x_2) = C_\theta(F_{X_1}(x_1), F_{X_2}(x_2)) = C_\theta(u, v), \tag{5.7}$$

where u and v are obtained by using the inverse probability integral transform [14]:

$$\begin{aligned} u &= F_{X_1}(x_1), \ u \sim \mathscr{U}(0, 1), \\ v &= F_{X_2}(x_2), \ v \sim \mathscr{U}(0, 1). \end{aligned} \tag{5.8}$$

From (5.7), it follows that copula $C_\theta(u, v)$ is a function that couples the marginal CDFs $F_{X_1}(x_1)$ and $F_{X_2}(x_2)$ of the random variable $X = (X_1, X_2)$ with its joint distribution $F_{X_1,X_2}(x_1, x_2)$.

From the large collection of bivariate copulas, the analysis in this book is focused on the Archimedean family, where copulas are constructed by using the following relation [15]:

$$C_\theta(u, v) = \varphi_\theta^{[-1]}(\varphi_\theta(u) + \varphi_\theta(v)), \tag{5.9}$$

where $u = F_{X_1}(x_1)$, $v = F_{X_2}(x_2)$, and $\varphi_\theta(\cdot)$ is called a generator function and $\varphi_\theta^{[-1]}(\cdot)$ is

$$\varphi_\theta^{[-1]}(t) = \begin{cases} \varphi_\theta^{-1}(t), & \text{if } 0 \leq t \leq \varphi_\theta(0); \\ 0, & \text{if } \varphi_\theta(0) \leq t \leq \infty. \end{cases} \tag{5.10}$$

The generator function $\varphi_\theta(t) : [0, 1] \rightarrow [0, \infty]$ must be continuous and strictly decreasing. Table 5.1 shows different types of Archimedean copulas constructed with the different generators $\varphi_\theta(t)$ [13]. Each of the families in Table 5.1 describes a

Table 5.1 Archimedean copulas

	$C_\theta(u,v)$	$\varphi_\theta(t)$	Solve $\left(\frac{\partial C_\theta(u,v)}{\partial u} = q, v\right)$
Clayton	$\left[\max\left(u^{-\theta}+v^{-\theta}-1,0\right)\right]^{-1/\theta}$	$\frac{1}{\theta}\left(t^{-\theta}-1\right)$	$(1-u^{-\theta}+(qu^{1+\theta})^{-\frac{\theta}{1+\theta}})^{-\frac{1}{\theta}}$
Frank	$-\frac{1}{\theta}\ln\left(1+\frac{(e^{-\theta u}-1)(e^{-\theta v}-1)}{e^{-\theta}-1}\right)$	$-\ln\frac{e^{-\theta t}-1}{e^{-\theta}-1}$	$\frac{1}{\theta}\log\frac{-e^{\theta}(1-q+qe^{\theta u})}{-e^{\theta}+qe^{\theta}-qe^{\theta u}}$
Gumbel–Hougaard	$\exp\left(-\left[(\ln u)^{\theta}+(-\ln v)^{\theta}\right]^{1/\theta}\right)$	$\ln\frac{1-\theta(1-t)}{t}$	Only numerical solution

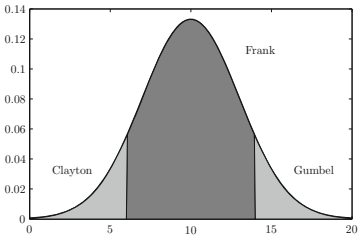

Fig. 5.1 Regions of best performance for different Archimedean copulas

different dependence structure. The selection is performed intuitively. As shown in Fig. 5.1, Clayton and Gumbel copulas exhibit the best results in the tails of the distribution, while Frank copula performs best under the bell of the distribution.

5.3.2 Estimation of the Parameter $\hat{\theta}$

The PDF and CDF are connected with the derivative (integral) relation. In terms of copulas, the joint CDF is $H(x,y) = C(u,v)$, hence to obtain the joint PDF one uses the relation

$$c(u,v) = \frac{\partial^2 C(u,v)}{\partial u \partial v}. \tag{5.11}$$

As an example, one may consider the Clayton copula. Starting from its CDF, one gets PDF as

$$c(u,v) = u^{-(\theta+1)}\left(-\frac{1+\theta}{\theta}\right)(u^{-\theta}+v^{-\theta}-1)^{-\frac{1+\theta}{\theta}-1}v^{-(\theta+1)}. \tag{5.12}$$

The rearrangement of the last equation leads to

$$c(u,v) = (1+\theta)(uv)^{-(\theta+1)}(u^{-\theta}+v^{-\theta}-1)^{-\frac{1+2\theta}{\theta}}. \tag{5.13}$$

One way to determine θ in (5.13) is through maximum likelihood estimation. By definition, the likelihood function of a random sample of size n is the joint probability density (mass) function denoted by [16]

$$L(\theta) = L(\theta; x_1, x_2, ..., x_n) = f(x_1, x_2, ..., x_n; \theta). \tag{5.14}$$

For a random sample consisting of independent, identically distributed random variables, (5.14) gets the form

$$L(\theta) = L(\theta; x_1, x_2, ..., x_n) = f(x_1; \theta) f(x_2; \theta) ... f(x_n; \theta), \tag{5.15}$$

where θ is a vector of parameters. In order to estimate $\hat{\theta}$ that maximizes the likelihood function (5.15), we take the derivative of $L(\theta)$ with respect to θ and set it equal to zero:

$$\frac{\partial L(\theta)}{\partial \theta} = 0. \tag{5.16}$$

The function $log(L(\theta))$ varies monotonically with its argument, or in other words, $log(L(\theta))$ increases and decreases when $L(\theta)$ increases and decreases respectively. This is because both functions are monotonically related to each other, leading to the same maximum estimate for both functions [17]. Hence, the maxima of the likelihood function and the logarithm of the likelihood function are the same. We use this fact in cases when it is easier to find the maxima of a logarithm likelihood function, such as when exponents are involved in the density function, as it is in our case. The logarithm of the density function $c(u, v)$ is

$$\log c(u, v) = \log(1 + \theta) - (\theta + 1) \log(uv) - \frac{1 + 2\theta}{\theta} \log(u^{-\theta} + v^{-\theta} - 1). \tag{5.17}$$

Finally, $\hat{\theta}$ is determined as the minimum negative log likelihood [18, 19]. The same procedure may be applied to all copulas that belong to the Archimedean family.

5.3.3 *Higher-Dimensional Copulas*

The copula, as defined by (5.7), couples two random variables into their joint CDF, hence the name bi-variate copula. However, the majority of problems are multidimensional, and thus, the bivariate copulas should be extended to accommodate multidimensional cases. There are two approaches to extending to higher dimensional copulas [4, 20]:

1. The first approach extends the bivariate copula to multivariate copula using only one dependence parameter θ. Such copulas are known as exchangeable Archimedean copulas [21]. The main drawback is that copulas for higher dimensions are tedious to derive [22].

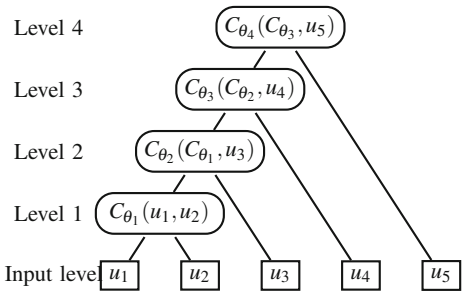

Fig. 5.2 Fully nested Archimedean copula

2. The second approach uses bivariate copulas to form a hierarchical structure with at most $n-1$ dependence parameters θ_i for n random variables. This construction of multivariate copulas is called a fully nested Archimedean copula (FNAC) [21, 23].

As shown in Fig. 5.2, a FNAC is a treelike structure that is obtained using an iterative procedure that starts with coupling two random variables. For this particular FNAC structure, u_1 and u_2 are coupled into copula $C_{\theta_1}(u_1, u_2)$ with parameter θ_1. In all subsequent iterations, the obtained copula is coupled with a new random variable; for example, copula C_{θ_1} is coupled with u_3 into $C_{\theta_2}(C_{\theta_1}, u_2)$ with parameter θ_2 and so on. The final output of the topmost copula reads

$$\begin{aligned} &C_{\theta_4}(u_1, u_2, u_3, u_4, u_5) = \\ &\quad = C_{\theta_4}\left(u_5, C_{\theta_3}\left(u_4, C_{\theta_2}\left(u_3, C_{\theta_1}\left(u_1, u_2\right)\right)\right)\right). \end{aligned} \tag{5.18}$$

Generally, a FNAC structure with n input variables has $n-1$ parameters θ_i. The final function (5.18) represents a valid copula only if the following condition is fulfilled [24]:

$$\theta_1 > \theta_2 > \cdots > \theta_{n-1}, \tag{5.19}$$

where θ_1 is the parameter of the most nested copula, θ_2 is the parameter of the second most nested copula, and so on. The estimations of the values of $\theta_i,\ i = 1, \ldots, n-1$ are obtained using the maximum likelihood algorithm.

Sometimes, it is not possible to build a FNAC structure that satisfies the condition (5.19) for the desired order of variables in the FNAC. In such a case, a valid FNAC could be found in the set of all FNACs obtained by permuting the order of the variables entering the FNAC [25].

5.4 Copula Based Condition Indicator

The process of computing the CI by using the impedance joint CDF is composed of several steps. First, from the available frequency range, a low cardinality frequency set is selected in a way that the fuel cell characteristic is preserved. Secondly, the

impedance values are calculated at the selected frequencies by using CWT (3.6). Afterwards, the parameters of the PDFs (3.13)–(3.18) are estimated by employing relation (3.20). It has to be noted that for each frequency f_i, the PDF of the wavelet coefficients (3.6) has different parameters. As a result, n different sets of parameters are calculated, one for each frequency f_i. In order to use the copula concept, the selected impedance values are transformed into a uniform random variable by using the CDF (3.19). Finally, the CI is computed as the output of the estimated multivariate copula.

5.4.1 Selection of the Appropriate Frequencies

Impedance is measured over a broad frequency range and the results are represented as a Nyquist plot. Usually, the number of selected frequencies is quite large. This number can be reduced by analysing a subset of frequencies that capture the generic shape of the Nyquist plot for the electrochemical device at hand. As an example, in the context of PEM fuel cells, the shape of the Nyquist plot suggests that the characteristic is predominantly capacitive, and it embodies two depressed semicircles:

- the low-frequency semicircle, which is attributed to diffusion processes, and
- the high-frequency semicircle, which is attributed to kinetic processes.

Therefore, it is reasonable to choose a similar number of impedance values from both frequency regions sampled at logarithmically equal intervals. As a result, the final feature set consists of N_f impedance values that preserve the information about the impedance shape. This feature set with reduced cardinality is subsequently used for the estimation of the system condition. A possible future improvement of the feature selection process can be achieved by employing, for instance, correlation-based feature selection methods, sequential forward (backward) feature selection, or minimum redundancy maximum relevance feature selection [26, 27].

5.4.2 Estimating Copula Parameters

For each impedance measurement, a complex matrix $Z(t,f)$ is obtained as a result of the CWT (2.24). The complex matrix $Z(t,f)$ has dimensions $m \times N_f$, where $m = \textit{sampling frequency} \times \textit{duration}$ is the number of time moments at which $u(t)$ and $i(t)$ were measured. The parameter N_f is the number of frequencies at which the impedance was measured.

By using the calculated impedance values at each of the selected frequencies f_i, $i = 1, \ldots, N_f$, the parameters (3.20) of the CDFs are estimated. Afterwards, using the corresponding CDF, each value of the matrix $Z(t,f)$ is transformed into its uniform feature. As a result, a matrix $\mathbf{U}$ with dimension $m \times N_f$ is obtained. Finally, the copula θ_i parameters (5.19) are estimated by employing the matrix $\mathbf{U}$.

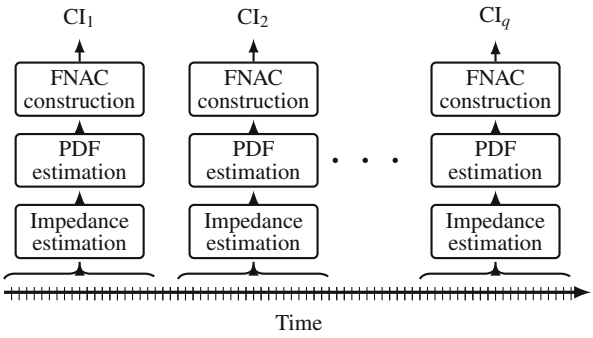

Fig. 5.3 Measurement sequences in time

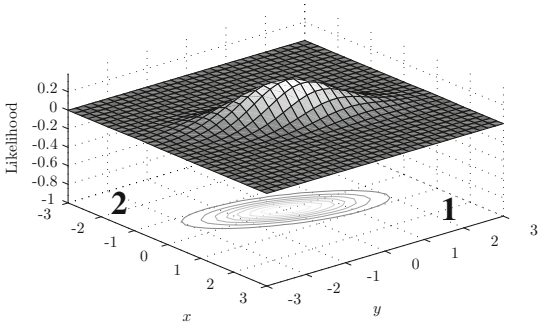

Fig. 5.4 Description of the regions for high and low copula outputs

5.4.3 Copula Output as an Aggregated Condition Indicator

Since the copula function is a CDF, its output is a probability of observing a particular combination of uniformly distributed values $\mathbf{U} = [u_1, \ldots, u_{N_f}]$. Through the experiment, for each measurement sequence q, a FNAC structure is built using uniform matrix $\mathbf{U}_q$. The process is shown in Fig. 5.3.

The calculated values from the initial fault-free measurements $q = 1$ are used as a baseline for CI. Since a deterioration in the condition will alter the impedance statistical characteristics, for the initially calculated copula, such a state will be regarded as a random event with a low likelihood. The low likelihood events (i.e., faults) lie in the tails of the PDF. As the output of CDFs is the probability $P[U \leq u]$, the output of the copula will be close to one for events that lie in the tail that is in the $(+, +, \ldots, +)$ hyperoctant.[1] On the other hand, the output of the copula will be close to zero for events that lie in the tail that is in the $(-, -, \ldots, -)$ hyperoctant. For a two-dimensional PDF, the $(+, +)$ quadrant is marked with 1 and the $(-, -)$ quadrant is marked with 2 in Fig. 5.4. The CI baseline will be located somewhere in between.

[1]The notation $(+, +, \ldots, +)$ specifies the area determined by positive semiaxes in all dimensions. A two-dimensional special case is shown in Fig. 5.4.

5.5 Summary

The derived analytical marginal PDFs allows the application of copula functions for data aggregation. As a result, information contained in the Nyquist plot, comprising the impedance values at an arbitrary frequency interval, can be reduced into an overall condition estimate. The condition of an electrochemical device is hidden in the dependence structure of the impedance values, which are, in the case of the fast EIS, complex random variables.

The resulting multidimensional CDF directly provides the probability of observing a certain form of the Nyquist plot with respect to the fault free one. Consequently, the calculated CI, defined as the output of the copula structure, is a probability of observing particular impedance values and is directly related to the electrochemical system condition as well as the severity of the present fault.

The proposed approach has several practical merits. First, for the purpose of fault detection, the proposed CI can be implemented without any prior characterisation of the electrochemical system under various faults. The CI baseline can be estimated from data acquired solely from measurements under a fault-free operation. Second, the approach is computationally efficient. Finally, the estimation of PDF parameters and the transformation of the acquired data into uniform random variables exist in closed form. This makes the proposed approach a suitable solution for an embedded CM system.

Determining the threshold values using the probability of false alarm has significant practical merit. For each of the measured impedance components one can calculate the probability of false alarm and use this value as an indicator of confidence that the current condition of the system has sufficiently departed from the fault free region. Furthermore, the proposed condition indicator scaled with the chosen PFA is directly related to the fault severity.

References

1. Bechhoefer, E., and A.P.F. Bernhard. 2007. A generalized process for optimal threshold setting in HUMS. In *IEEE aerospace conference*.
2. Silverman, B.W. 1986. *Densiy estimation for statistics and data analysis*. New York: Chapman and Hall.
3. Al-Harthy, M., S. Begg, and R.B. Bratvold. 2007. Copulas: A new technique to model dependence in petroleum decision making. *Journal of Petroleum Science and Engineering* 57 (1–2): 195–208.
4. Fischer, Matthias, Christian Kock, Stephan Schluter, and Florian Weigert. 2009. An empirical analysis of multivariate copula models. *Quantitative Finance* 9 (7): 839–854.
5. Bouyé, E., V. Durrleman, A. Nikeghbaliand, G. Riboulet, and T. Roncalli. 2000. Copulas for finance - a reading guide and some applications. doi:10.2139/ssrn.1032533.
6. Genest, C., and A.C. Favre. 2007. Everything you always wanted to know about copula modeling but were afraid to ask. *Journal of Hydrologic Engineering*.
7. Kim, J.M., Y.S. Jung, E.A. Sungur, K.H. Han, C. Park, and I. Sohn. 2008. A copula method for modeling directional dependence of genes. *BMC Bioinformatics*.

8. Mercier, G., G. Moser, and S.B. Serpico. 2008. Conditional copulas for change detection in heterogeneous remote sensing images. *IEEE Transactions on Geoscience and Remote Sensing* 46 (5): 1428–1441.
9. Mileva Boshkoska, B., M. Bohanec, P. Boškoski, and Đ. Juričić. 2015. Copula-based decision support system for quality ranking in the manufacturing of electronically commutated motors. *Journal of Intelligent Manufacturing* 26 (2): 281–293. doi:10.1007/s10845-013-0781-7.
10. Jaimungal, S., and K.H.Ng. Eddie. 2009. Kernel-based copula processes. In *ECML PKDD 2009*, pp. 628–643.
11. Sklar, Abe. 1973. Random variables, joint distribution functions, and copulas. *Kibernetika* 9.
12. Sklar, A. 1996. *Distributions with fixed marginals and related topics - random variables, distribution functions, and copulas - a personal look backward and forward*, vol. 28. Hayward: Institute of Mathematical Statistics.
13. Nelsen, Roger B. 2006. *An introduction to copulas*, 2nd ed. New York: Springer.
14. Leemis, Lawrence M., and Stephen K. Park. 2005. *Discrete-event simulation: A first course*. USA: Prentice-Hall Inc.
15. Joe, Harry. 1997. *Multivariate models and dependence concepts*. New York: Chapman and Hall.
16. Martinez, Wendy L., and Angel R. Martinez. 2002. *Computational statistics handbook with matlab*. Boca Raton: Chapman and Hall.
17. Myung, I.J. 2003. Tutorial on maximum likelihood estimation. *Journal of Mathematical Psychology* 47: 90–100.
18. Brent, Richard. 1993. *Algorithms for minimization without derivatives*. Englewood Cliffs: Prentice-Hall.
19. Forsythe, G., M. Malcolm, and C. Moler. 1976. *Computer methods for mathematical computations*. Englewood Cliffs: Prentice-Hall.
20. Savu, C., and M. Trade. 2006. Hierarchical archimedean copulas. In *International conference on high frequency finance*, Konstanz, Germany
21. Berg, Daniel, and Kjersti Aas. 2009. Models for construction of multivariate dependance: A comparison study. *European Journal of Finance* 15 (7–8): 639–659.
22. Trivedi, Pravin, and Zimmer David. 2006. *Copula modeling: An introduction for practitioners*. Hackensack: World Scientific Publishing.
23. Hofert, Marius. 2010. Construction and sampling of nested archimedean copulas. *Copula theory and its applications, Proceedings of the workshop held in Warsaw 25–26 September, 2009*, 147–160. Lecture notes in statistics Heidelberg: Springer.
24. Rachev, S.T. (ed.). 2003. *Handbook of heavy tailed distributions in finance*. Amsterdam: Elsevier/North Holland.
25. Mileva Boshkoska, B., and M. Bohanec. 2012. A method for ranking non-linear qualitative decision preferences using copulas. *International Journal of Decision Support System Technology* 4 (2): 42–58. doi:10.4018/jdsst.2012040103.
26. Onanena, R., L. Oukhellou, D. Candusso, F. Harel, D. Hissel, and P. Aknin. 2011. Fuel cells static and dynamic characterizations as tools for the estimation of their ageing time. *International Journal of Hydrogen Energy* 36 (2): 1730–1739. doi:10.1016/j.ijhydene.2010.10.064.
27. Benouioua, D., D. Candusso, F. Harel, and L. Oukhellou. 2014. PEMFC stack voltage singularity measurement and fault classification. *International Journal of Hydrogen Energy* 39 (36): 21631–21637. doi:10.1016/j.ijhydene.2014.09.117.

Chapter 6
Condition Monitoring of PEM Fuel Cells

In order to show the potential of the proposed CM method beyond laboratory usage, this chapter presents the complete process of tuning and evaluation of a CM system for a PEM fuel cell under various water management faults. The evaluation was performed on a commercially available PEM fuel cell system, the HyPM HD 8 produced by the Hydrogenics Corporation. The stack consists of 80 PEM fuel cells each with a surface area of 200 cm^2, providing 8.5 kW of electric power in total. The fuel cell system operates on pure hydrogen and ambient air.

6.1 Experimental Setup

The electronic load was connected to the fuel cell system and it was used to perturb the system with a DRBS perturbation signal in galvanostatic mode. The waveform of the load current was controlled by an arbitrary function generator. The generator was generating the DRBS reference signal, which was feed to the electronic load as a reference signal for the load current. The block diagram in Fig. 6.1 presents the experimental setup. In the presented configuration, all signal flows can be distinctly observed.

For the impedance calculation, the voltage of each cell of the stack was measured separately using a 90 channel fuel cell voltage monitor (FCVM). An FCVM provides wide frequency measurements of the electrical current delivered by the fuel cell stack as well as the corresponding voltages of each individual stack. The details about the hardware implementation of the FCVM are given in Chap. 7.

P. Boškoski et al., *Fast Electrochemical Impedance Spectroscopy*,
SpringerBriefs in Applied Sciences and Technology,
DOI 10.1007/978-3-319-53390-2_6

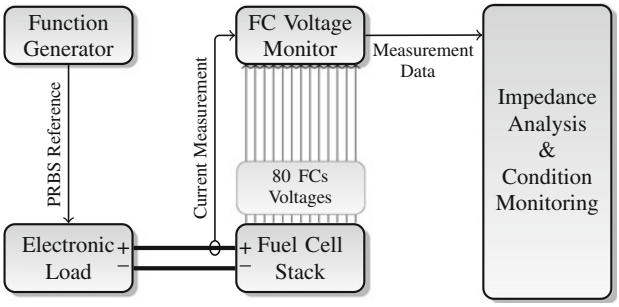

Fig. 6.1 Block diagram of the experimental setup

6.2 Experimental Profile

Two types of artificial faults were included in the evaluation process, i.e., flooding and drying of the stack. The rationale behind the selection of these two faults is twofold. First, both faults are short term and more importantly reversible. Secondly, they have a profound effect on the fuel cell performance. Therefore, the changes in the fuel cell condition are sufficiently fast and the performance of the proposed CI can be promptly evaluated. The experiment went through five stages:

1. nominal inlet air humidity for 11 min,
2. dried inlet air for 10 min,
3. nominal inlet air humidity for 10 min,
4. 100% humid inlet air for 10 min, and
5. nominal inlet air for the last measurements.

The interim inlet air with nominal humidity was fed in order to cancel the influence of the previous fault and monitor the recovery of the fuel cell. According to the procedure described in Chap. 5, the electrical current and voltage were sampled with frequency $f_s = 5$ kHz. A single data acquisition segment lasted 60 s. Measurements were performed 40 s apart.

In the stages with nominal air humidity, the relative humidity of the inlet air was kept at 9% (which at 50°C corresponds to 7.5 g/m^3 - grams of water per cubic meter of air). In order to induce drying, air fed to the fuel cell was slightly dried down to a relative humidity of 5% (4.1 g/m^3) for about 10 min, between the 12th and the 22nd min. The first interim "recovery" period was between the 22nd and the 34th min. The flooding was introduced between the 34th and the 58th min. During that time, saturated air with a relative humidity of 100% (83 g/m^3), was fed into the fuel cell system inducing flooding of the fuel cells. At the final stage, the air humidity was decreased down to the initial 9%.

6.3 Time Evolution of Particular Impedance Components at a Single Frequency

The impedance values were calculated according to the fast EIS procedure described in Chap. 2. The analysis was performed in the frequency band [0.5, 500] Hz. The thresholds in the plots in Fig. 6.3 were calculated according to (5.1) for four PFA values $PFA = \{25, 20, 15, 10\%\}$ using the corresponding CDFs (3.16) and (3.19). The corresponding parameters σ_u, σ_i and ρ were estimated from the fault free signals during the first stage of the experiment by employing (3.20). The histogram of the impedance components from the first stage of the experiment are shown in Fig. 6.2. The plots additionally show the theoretical PDFs using the estimated parameters σ_u, σ_i and ρ. It is clearly visible that the theoretical PDFs closely describe the empirically calculated histograms.

The time evolution of the impedance at 153 Hz is shown in Fig. 6.3. The changes in the impedance values clearly indicate the five experiment stages. The first departure from the fault free condition was between the 12$^{\text{th}}$ and the 22$^{\text{nd}}$ min when the fuel cell was fed with somewhat drier air (5% relative humidity). In that particular region, the real component of the impedance increased and surpassed the threshold of 70%, as shown in Fig. 6.3a, b. A similar observation can also be made for the module of the impedance, as shown in Fig. 6.3c. Despite the minute changes in the relative humidity of the inflow air, there is an apparent change in the value of the impedance, with 30% probability of false alarm. Without the threshold values, such a quantification would have been impossible.

Unlike the minor changes caused by the mild decrease in the humidity, the flooding with 100% saturated air inflow shows significant changes in all three impedance components. The values of $\Re(z)$ and $|z|$, between the 34$^{\text{th}}$ and the 58$^{\text{th}}$ minute, indicate that the condition of the fuel cell departed from the fault free area, with less than 10% probability of false alarm, as shown in Figs. 6.3a and c. The change in the imaginary component $\Im(z)$ is somewhat smaller; the probability of false alarm is less than 30%. Finally, when the relative humidity of the air inflow was returned to normal, the impedance components returned to the initial values within the fault free region.

6.4 Time Evolution of the Condition Indicator at a Single Frequency

Following the procedure described in Sect. 5.2, a CI based on the impedance module $|z|$ was calculated for each measurement. Its time evolution is shown in Fig. 6.4. The values of the CI were calculated using the mapping relation (5.4) with $PFA = 90\%$.

By analysing this time evolution, one can notice that during the fault free operation the CI acquires low values. As the first fault was induced, the values of the CI increased up to 0.5, which indicates that the condition of the fuel cell deteriorated.

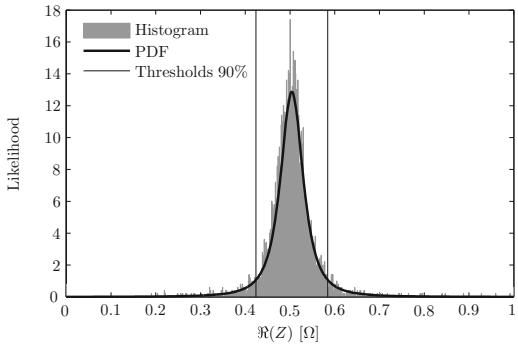

(a) Distribution of $\Re(Z)$

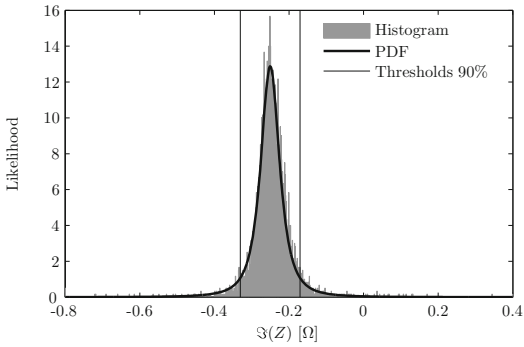

(b) Distribution of $\Im(Z)$

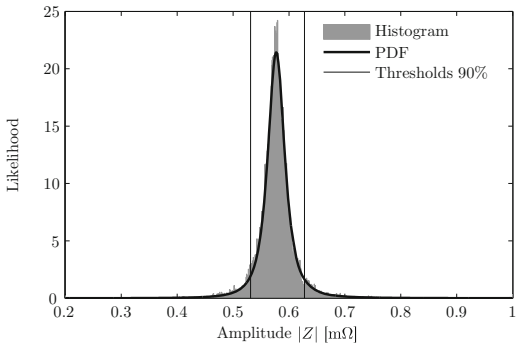

(c) Distribution function of the module of the impedance

Fig. 6.2 Probability distribution functions of particular impedance components

The acquired value of 0.5 clearly shows departure from fault free operation, while at the same time is inline with the low severity of the induced drying, relative humidity change of 8%. Unlike the low severity of the drying fault, during the flooding phase of the experiment, the value of CI surpasses the limit value of 1. The overwhelming

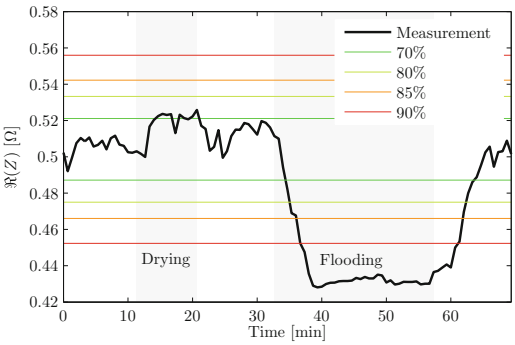

(a) Values of $\Re(Z)$

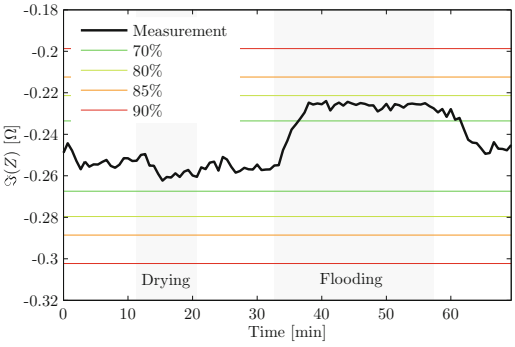

(b) Values of $\Im(Z)$

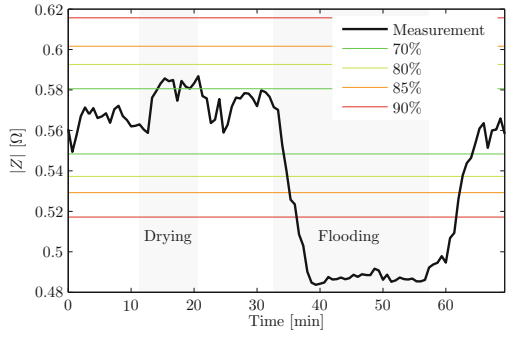

(c) Values of $|Z|$

Fig. 6.3 Trend of impedance components throughout the experiment

flooding of the system is directly reflected in the high value of the CI. Finally, at the end of the experiment, when the air condition was back to nominal, the values of the CI decreased indicating almost fault free operation.

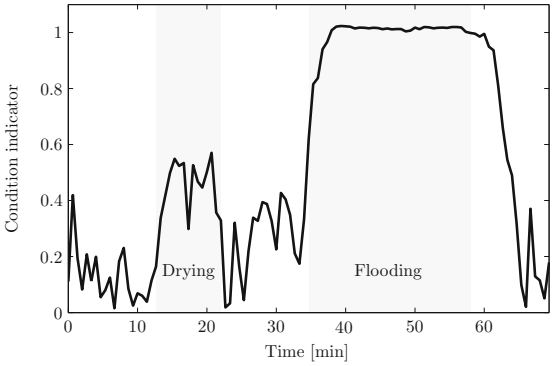

Fig. 6.4 Trend of CI of $|Z|$ throughout the experiment

The results confirm the behaviour of the CI. It is sufficiently sensitive on deviation in the condition of the water management. At the same time, its value is directly related to the severity of the deviation with respect to the selected PFA.

6.5 Time Evolution of the Aggregated Condition Indicator

Following the procedure described in Sect. 5.4, the CI was computed for each of the $q \in [1, 105]$ measurements. The time evolution of the CI is presented in Fig. 6.5, where the experiment time is represented on the x-axis.

At the beginning of the experiment, the copula value defines the CI baseline of a fault-free condition. Dry inlet air of 5% relative humidity causes fuel cells to dry out, hence the increase of the CI. This indicates that some of the impedance components changed, and consequently, the observed measurements belong to a low likelihood tail. On the other hand, the saturated inlet air with a relative humidity of 100% causes the flooding of fuel cells. As a result, the CI reaches almost zero. At the end of the experiment, the humidity of the inlet air was set back to nominal values, resulting in

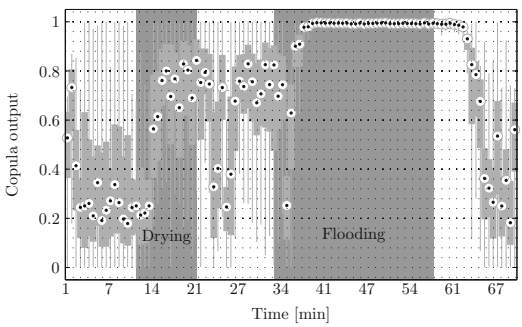

Fig. 6.5 Evolution of the condition indicator (copula output)

fuel cell recovery, causing the CI to return to the baseline values similar to the values from the beginning of the experiment.

It has to be noted that the experiment was performed on an industrial-grade fuel cell system. As such, the built-in controls managed various parameters such as air and fuel flow (stoichiometry) as well as temperature. Therefore, these parameters were not strictly held within sharp boundaries with laboratory precision. As a result, some fluctuations can be observed in the CI values throughout the experiment (Fig. 6.5). Regardless of these fluctuations, the fault regions are distinctly visible, which confirms the link between the CI and the actual fuel cell condition.

The results show that the proposed CI (i.e., copula output) can also be directly related to the fault severity. The departure of the copula values for the drying fault from the baseline level is smaller compared with the copula values during the flooding fault, which corresponds to the induced fault severity.

6.6 Summary

The results in this chapter are a clear presentation of the applicability of the proposed fast EIS approach for CM of electrochemical energy systems. Furthermore, it is shown that real-world measurements conform with the theoretical results. The capability of setting accurate diagnostic thresholds based solely on fault free operation significantly diminishes the commissioning efforts and increases the practicality and reliability of the proposed CM approach. The final chapter of this book will present a complete, production ready, embedded CM system for PEM fuel cells based on the proposed fast EIS approach.

Chapter 7
Hardware Components for Condition Monitoring of PEM Fuel Cells

The fast EIS technique presented in the previous chapters is a generic tool applicable to various electrochemical devices. The biggest obstacle for real-world implementation is the available data acquisition equipment. Usually, impedance measurement devices are predominantly designed for laboratory usage (i.e., frequency response analysers) and therefore are unsuitable for online CM applications.

Typically, when performing EIS on an operational device, the device is disconnected from the load and the procedure of applying the excitation signals and the actual measurement are performed offline. Addressing this issue, this chapter presents a hardware solution for CM of PEM fuel cell systems capable of performing fast EIS without interrupting the normal operation of the electrochemical device under test.

The proposed hardware setup consists of a modular step-down direct-current-to-direct-current (DC-DC) converter and a 90-channel fuel cell voltage monitor. Besides its basic capability of electric power conversion, the DC-DC converter is capable of injecting current excitation signals of arbitrary waveform to the input device (i.e., PEM fuel cell stack). On the other side, the designed voltage monitor enables precise voltage measurement of all individual cells in the fuel cell stack. The interconnection between the DC-DC converter and the voltage monitor provides a platform for an embedded CM system that can operate in online mode without interrupting the normal operation of the underlying electrochemical system. The architecture of the designed system is presented in Fig. 7.1.

7.1 DC-DC Converter

Contemporary commercial fuel cell systems are equipped with DC-DC converters and voltage monitors that fulfil only basic requirements for output power conditioning (e.g., [1–9]) and monitoring (e.g., [10, 11]). The designed DC-DC converter is a

P. Boškoski et al., *Fast Electrochemical Impedance Spectroscopy*,
SpringerBriefs in Applied Sciences and Technology,
DOI 10.1007/978-3-319-53390-2_7

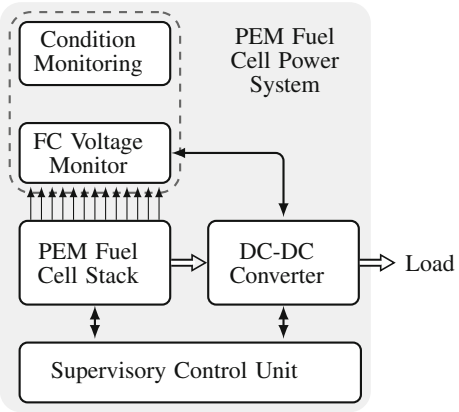

Fig. 7.1 Block diagram of a PEM fuel cell power system

conversion module that converts the output voltage of a fuel cell power module into the voltage of an energy storage device (e.g., rechargeable lithium battery or storage capacitor). The input device (i.e., fuel cell stack) and the output device (i.e., secondary battery) are current source and current drain, respectively. Therefore, the DC-DC converter should be treated and designed as a current-transforming device. Yet, this is uncommon for nearly all commercially available converters, which mostly operate as voltage-transforming devices.

Having a DC-DC converter as a current-transforming device makes the stack current under the primary control variable, while the stack voltage is monitored in order to ensure safety and operation in an appropriate range. The same applies to the output side, where the current is under primary control, and the output voltage is supervised in order to stay in the predefined range.

To achieve high conversion efficiency, topology with the lowest number of power components is preferred. The conversion topology employed is the step-down converter. For such a converter, the main energy flow goes only through a single-pole, double-throw, electronic switch and the power inductor. As a result, only a small amount of energy is cycled in the power inductor during each conversion cycle.

Given the current mode of operation, several DC-DC converter modules can be paralleled to obtain higher output currents. The external master controller can be programmed to dynamically share the load between several parallel converters in order to fulfil the current load requirements and to optimise the efficiency of conversion. At low current loads, the master controller can switch off some of the modules and drive the others to a higher conversion power. In this way, the switching losses of the less loaded modules are eliminated and the overall conversion efficiency is increased.

In the present configuration, the solution is limited to a maximum of eight parallel DC-DC converter modules, each handling up to 80 A of output current. When eight units are paralleled, the overall current reaches up to 640 A, attaining the capacity of power conversion of nearly 16 kW in 24 V systems. An example of an implemented

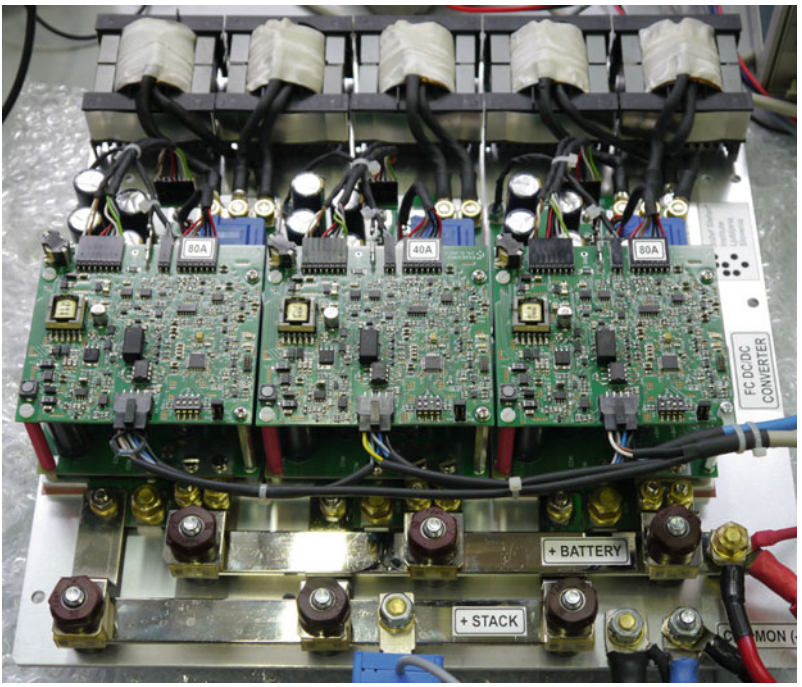

Fig. 7.2 Assembly of three DC-DC converter modules paralleled together providing 5 kW of power conversion capability

5 kW conversion block is shown in Fig. 7.2. The assembly consists of three parallel DC-DC converter modules, two capable of delivering 80 A and one 40 A of current.

By paralleling several DC-DC converter modules, a lower input current ripple is achieved by the asynchronously operated modules. The current mode step-down converter with constant OFF-time inherently operates with variable frequency. As confirmed by the performed test, three paralleled modules have never fallen into synchronism, even if they were driven by the same current set-point. This allows further optimization (i.e., reduction) of the size of the input capacitor bank.

The block diagram in Fig. 7.3 depicts the conceptual arrangement of the DC-DC module. Roughly, the module can be divided into three functional blocks, namely,

- multichannel power supply,
- microcontroller circuitry, and
- step-down power output stage.

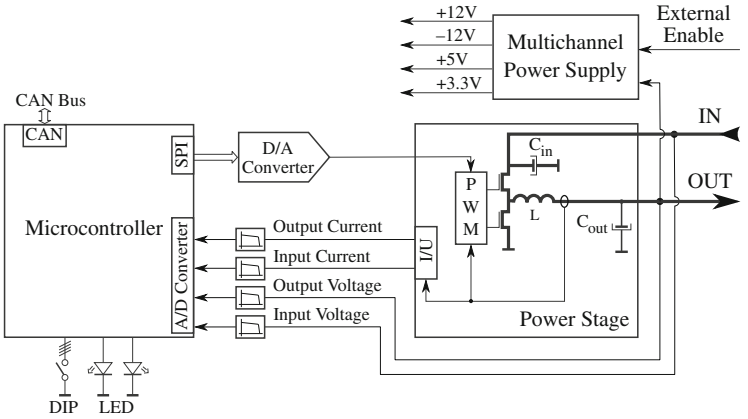

Fig. 7.3 Block diagram of the DC-DC module

7.1.1 Microcontroller Circuitry

The microcontroller circuitry is powered by a multichannel power supply. The supply voltages are generated by a fly-back converter topology. The multichannel power supply must be enabled by an external digital signal. With this signal, the external master controller can switch ON or OFF the complete DC-DC converter module. This enables isolation of the defective module as well as increases in the efficiency of operation at low loads.

The DC-DC module is managed over a controller area network (CAN) communication bus. The primary task of the microcontroller is to receive CAN messages with set-point values for the DC-DC converter and to adjust the peak current of the output stage accordingly. The set-points that can be sent to the microcontroller of a DC-DC converter module via the CAN bus are (i) the peak value of the output current, (ii) the maximum output voltage, (iii) the amplitude of the excitation signal for the impedance measurements, and (iv) the frequency of the excitation signal. The only way the embedded microcontroller can affect the power stage is by means of a control signal through an external 12-bit D/A converter. The microcontroller supervises the operation of the DC-DC conversion across four analogue inputs (see Fig. 7.3).

7.1.2 Power Output Stage

The step-down power output stage is designed as a self-sufficient block. It needs no microcontroller intervention to oscillate and to control the output current. Hence, the safety of the power control is not affected by possible software errors or strong

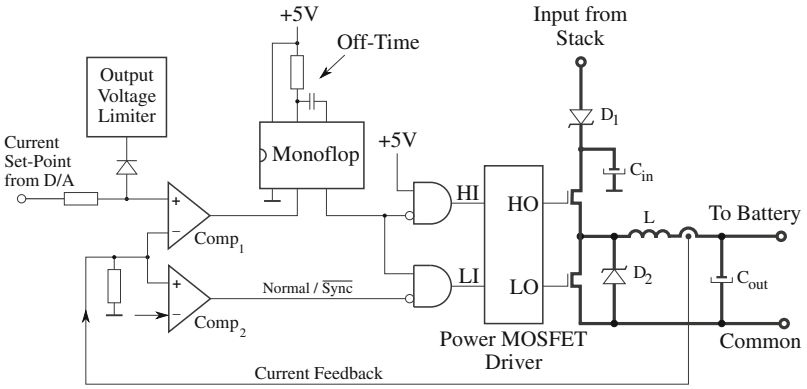

Fig. 7.4 Power output stage of DC-DC converter

external transients, which would cause the microcontroller to operate temporarily in an undefined state.

The energy flow of the power output stage of the DC-DC converter is controlled by pulse-width modulation (PWM). The design of the output stage is presented in Fig. 7.4. PWM cycles power metal-oxide-semiconductor field-effect transistors (MOSFETs) in a synchronous mode. This mode reduces power dissipation during the OFF cycle of the converter. The power inductor L filters the modulating current variations and, together with the output capacitor C_{out}, provides necessary low-pass filtering. Input current variations are filtered out with an input capacitor bank C_{in}, which eliminates fuel cell stack current ripple. Stack current is delivered through the Schottky diode D_1 intended to prevent back current flow that would otherwise cause irreparable damage to the fuel cell stack.

The standard current mode converter with constant frequency is most often employed, although it suffers from inherent low-frequency instability [12–15]. As the stack voltage is frequently close to the required output voltage, the DC-DC conversion is subjected to operation at high PWM duty cycles. The constant-OFF mode of the current control is a particularly convenient method for this purpose. Therefore, at the design of the DC-DC converter, a *current mode step-down converter with a constant OFF-time and synchronous switching mode* was used. The constant-OFF type encounters no inherent instability problems and enables cycle-by-cycle peak current control of the output stage.

Figure 7.4 shows that the output pair of N-type MOSFETs is driven by a high-side/low-side MOSFET driver. When the upper MOSFET bank is switched ON, electrical current starts to flow from the fuel cell stack and the input capacitor bank into the output capacitor bank and the load. The current in the inductor increases until the current sensor detects a set-point value, as shown in Fig. 7.5. When output current exceeds the set-point value, the Comp_1 triggers the monostable flip-flop. This causes the top MOSFET bank to switch OFF and the bottom MOSFET bank to switch ON (the driving signals for the MOSFET banks are shown in Fig. 7.5). The

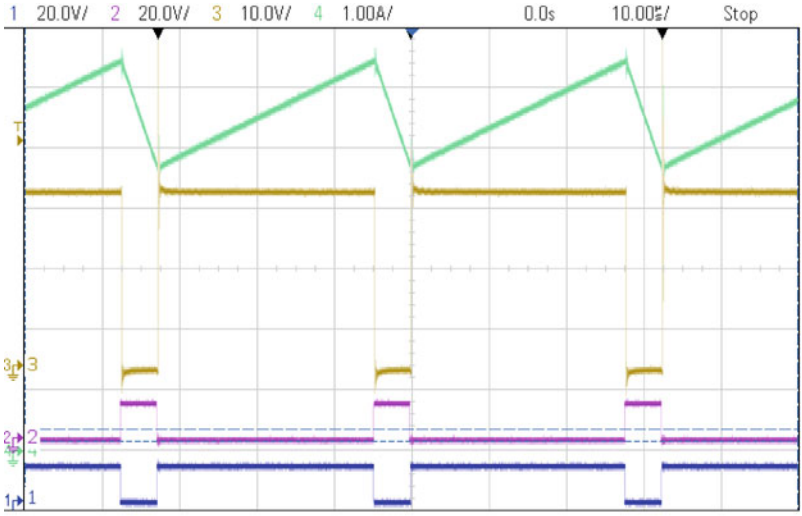

(a) U_{in} = 32 V, I_{out} = 5.5 A

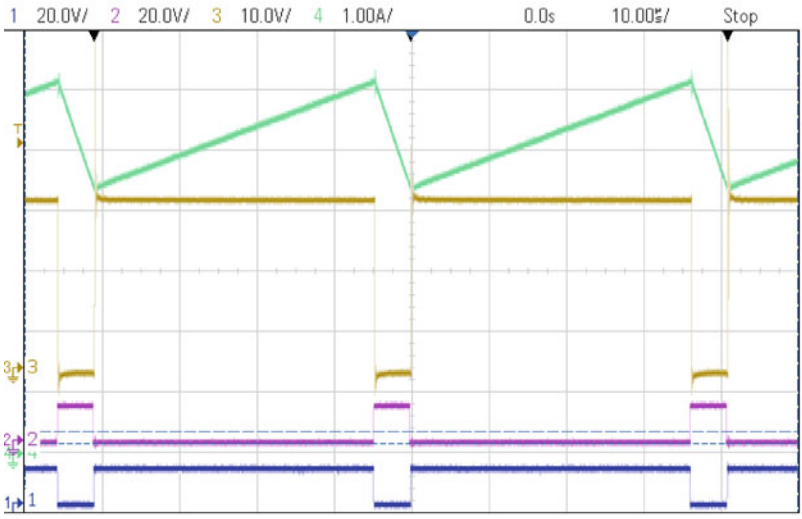

(b) U_{in} = 28 V, I_{out} = 5.5 A

Fig. 7.5 Key waveforms of the DC-DC converter operating at two different input voltages U_{in} and the same output current I_{out} (CH1 [*blue*]: LI signal, CH2 [*magenta*]: HI signal, CH3 [*brown*]: voltage of the power inductor's entry point, CH4 [*cyan*]: power inductor current)

inductor current recirculates through the lower transistor bank and decreases linearly for a defined amount of time (constant-OFF). When the predefined time elapses, the top MOSFETs switch ON again and allow the passage of stack current to the output.

The OFF-time is determined by the RC constant of the monoflop constant. The ON-time is variable and depends on the input voltage. If the input voltage from the stack is high, the ON-time becomes short, and vice versa. When the input voltage approaches the output voltage, the oscillation ceases away, and the current goes straight through. With the present design, the OFF-time is set to 4 μs. When the fuel cell stack output voltage is near twice the required DC-DC converter output voltage, the output stage oscillates at 125 kHz. The switching frequency increases with the input-output voltage ratio. When the input voltage is only a few volts above the output voltage, the switching frequency drops to a few kilohertz. At the ultimate situation, the switching stops completely. In this way, a very wide range of input voltages are covered. Given the backflow protection diode D_1, the input voltage must be at least one diode drop higher than the output voltage. To illustrate the constant-OFF mode, the waveforms shown in Fig. 7.5 were acquired under the same output current I_{out} but at two different input voltages U_{in}. The OFF-time is identical in both cases, whereas the ON-time is longer in the case of lower input voltage U_{in} (i.e., Fig. 7.5b) in order to fulfill the requirements of the output current.

When a battery is connected to the output of the converter, the implementation of the synchronous mode is not a straightforward task. The backflow current might flow from the battery back through the power inductor and the lower bank of MOSFETs (e.g., at zero current set-point). In such a case, the inductor current would rise to values at which the circuitry would be damaged instantly. To avoid this, the circuitry actually switches between the normal mode (when the diode D_2 is used to recirculate the inductor current) and the synchronous mode (when low-side MOSFETs are used instead). The switchover is performed by the comparator Comp_2. At low output currents, the output stage operates in normal mode, and lower MOSFETs are never switched ON. At higher output currents, the synchronous mode takes over and keeps the switching losses low.

The DC-DC converter strictly operates in current-transforming mode. However, when the output voltage reaches the gassing level of the battery, the output current is reduced. In this situation, the output voltage limiter (see Fig. 7.4) reduces the current set-point. It operates as a secondary voltage control loop and fixes the battery voltage at the set-value by forcing lower output current as demanded.

7.2 Fuel Cell Voltage Monitor

A significant voltage drop is an indication that either the operating conditions or the health of the fuel cell is seriously impaired. Therefore, even low-cost, fuel cell-based power systems require some kind of cell voltage monitoring. A significant discrepancy exists between the laboratory-grade and the commercially available diagnostic and measurement equipment. The trade-off is between the capability of handling fast and precise measurements on the one hand and the price on the other [16, 17]. Most of the commercially installed FCVM systems are capable of measuring only the joint voltage of two or more adjacent fuel cells with a rather low sample rate and

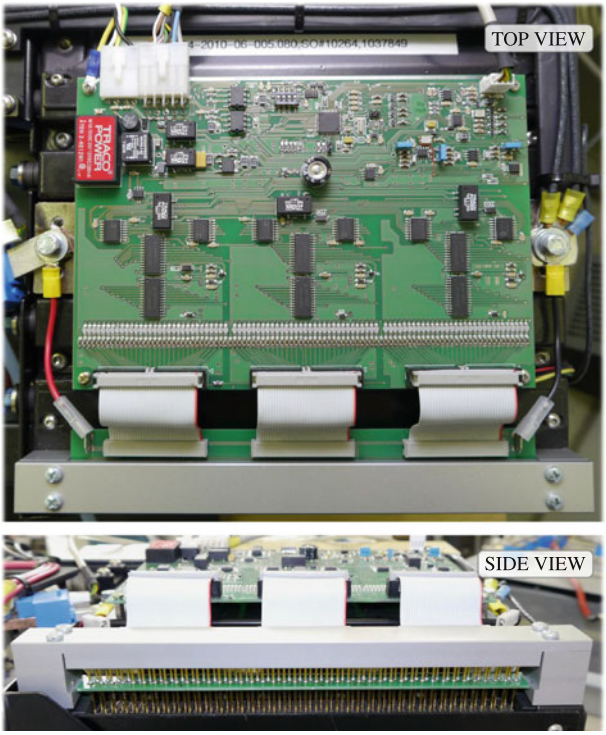

Fig. 7.6 FCVM connected to an 8.5 kW PEM fuel cell system Hydrogenics HyPM-HD 8-200 (*top view* FCVM's PCB; *side view* realization of contacts to all of the fuel cells)

resolution. Notwithstanding the cost-effectiveness, such equipment suffices only for detecting severe deteriorations in the fuel cell condition. As a result, it is incapable of performing total stack monitoring or providing more sophisticated diagnostic information.

The proposed solution bridges the gap between the laboratory-grade measurement equipment and the contemporary commercial diagnostic systems. The proposed FCVM is a low-cost data acquisition device capable of performing a precise voltage measurement of individual cells inside a fuel cell stack that consists of up to 90 cells. Additionally, it provides a platform for conducting EIS measurements on every cell of the stack. Figure 7.6 shows a typical implementation of the FCVM connected to a PEM fuel cell stack of a commercially available power unit via spring contact pins.

7.2.1 *Resolving the High Common-Mode Voltage Potential Issue*

One of the biggest issues when measuring the voltage of an individual cell within a larger stack is a high common-mode potential, which builds up from the potentially low cell to the highest cell in the stack. The signal acquisition system must be capable of measuring only a few millivolts superimposed on several tens of volts. Such a high common-mode potential poses two limiting factors: the ability of a multiplexer to select the individual cell within this very wide common-mode voltage range and the ability of instrumentation amplifiers or floating A/D converters to extract the relatively small cell voltage in the presence of high voltage offset [18].

The issue of high common-mode voltage range of multiplexers remains unsolved by readily available low-cost measurement devices. The proposed solution employs standard CMOS analogue multiplexers. By proper biasing and using an isolated DC-DC power supply, making a floating analogue multiplexer is possible. Figure 7.7 shows that an isolated DC-DC converter provides voltage supply to the multiplexer. Two Zener diodes regulate the bias for the multiplexer for maximum input range, while an NPN transistor supplies current to a digital signal isolator, which selects the particular input. The selected voltage is then transferred to the difference amplifier for further signal preparation and A/D conversion. One such circuitry is capable of handling signals from up to 30 fuel cells.

To decrease the number of multiplexers, two multiplexers are interlaced as shown in Fig. 7.8. In this way, only one input is effectively used per cell. Thus, selecting 30 cells is possible by using a pair of standard 16-to-1 multiplexers. One spare channel is used for automatic autozero measurement, which eliminates the offset voltage of the difference amplifier.

An ARM Cortex-based microcontroller performs synchronization among different AD channels required for proper data acquisition. Additionally, the microcontroller controls the communication interfaces and provides the necessary computational resources for the execution of the diagnostic algorithms.

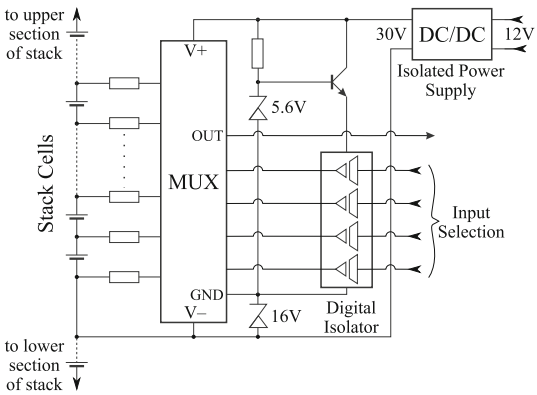

Fig. 7.7 Floating power supply scheme, which allows an industry-standard multiplexer to operate in floating mode

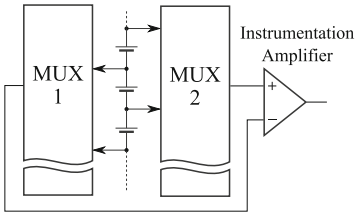

Fig. 7.8 Connection of two industry-standard multiplexers to measure up to 30 fuel cell leads in order to reduce component count

7.2.2 FCVM Measurement Modes

The FCVM can perform two types of measurements:

- voltage monitoring of all the cells of the stack and
- impedance measurement of individual cells.

In the first mode, the FCVM measures the voltage of each individual cell inside a stack with a resolution of 62.5 μV. The stack voltage and current are also measured with a resolution of 24 mV and 10 mA, respectively. The stack voltage and current are measured through a simple voltage divider and Hall-effect current transducer, respectively. In the monitoring mode, the refresh rate is 400 ms.

The second measurement mode provides a powerful tool for performing measurements intended for EIS-based diagnostics. The relevant AC diagnostic signals are superimposed on the operational DC signals of the fuel cell and have small amplitudes with respect to the DC component. Measuring such low-amplitude AC signals at low noise is of utmost importance.

To achieve the required high resolution at low noise, the voltage of an individual cell undergoes two preprocessing steps. In the first step, the DC component is subtracted by employing the analogue subtraction circuit. In the second step, the remaining AC component of the signal is amplified by a factor of 10 in order to attain low noise and a higher resolution of A/D conversion, as shown in Fig. 7.9. Consequently, the FCVM measures the AC voltage of sequentially selected cells inside a stack with a high resolution of 80 μV at a sampling rate of 5 kHz. Special care was taken to keep the frequency response of voltage and current measuring paths as equal as possible as the impedance is actually proportional to their ratio in the amplitude/phase space.

Normally, extraction of AC signals in the presence of a DC signal is performed by using a high-pass analogue filter. However, switching among cells would cause a long settling time of the filter, which would significantly prolong the data acquisition time. Since the DC voltage of the cell obtained by the first measuring mode is already known to the microcontroller, the value is sent to the subtraction circuitry via the D/A converter, as shown in Fig. 7.9. The result is the AC component of the signal with a small DC residue caused by circuit imperfections and slow cell voltage variations. This composite signal is then amplified to gain higher resolution and to keep a high signal-to-noise ratio. As the DC residue is also amplified, it is removed later by digital signal processing within the microcontroller.

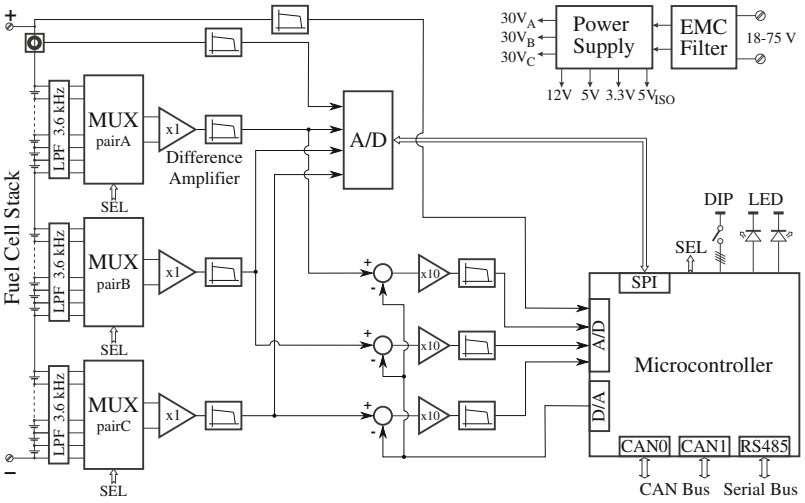

Fig. 7.9 Block diagram of the FCVM

7.2.3 DC-DC Converter and FCVM as a Condition Monitoring System

To perform online EIS-based CM of PEM fuel cells, the DC-DC converter module and the FCVM were interconnected into a CM system. The interconnection enables the performing of measurements that are required for the fast EIS technique. The FCVM performs the voltage and current measurements, and conducts the signal processing tasks. The DC-DC converter performs the DC-DC conversion, and when prompted by the FCVM, it executes the current excitation of the fuel cells. The scheme of the interconnected condition monitoring system is shown in Fig. 7.10.

To perform the current excitation of the cells, the DC-DC converter module is equipped with a firmware-based excitation pattern generator, as shown in Fig. 7.10. Using the selected pattern, the microcontroller modulates the output current of the DC-DC converter. As this variation of the output current is filtered out by the output capacitor bank, the modulation does not significantly affect the load. On the input side of the DC-DC converter, the current modulation affects the current through the fuel cell stack. The stack becomes excited enough to respond with minute variations of the cells' voltages. By measuring these variations with the FCVM, the information on the impedance of the cells is obtained.

The excitation of the electrochemical device is affected by the presence of the input capacitor bank of the DC-DC converter and its dynamics. The capacitor bank must be present to reduce stack current ripple. This capacitance is paralleled to the stack, and its influence is most prominent at high frequencies, while the information on the cells' condition is present at low frequencies.

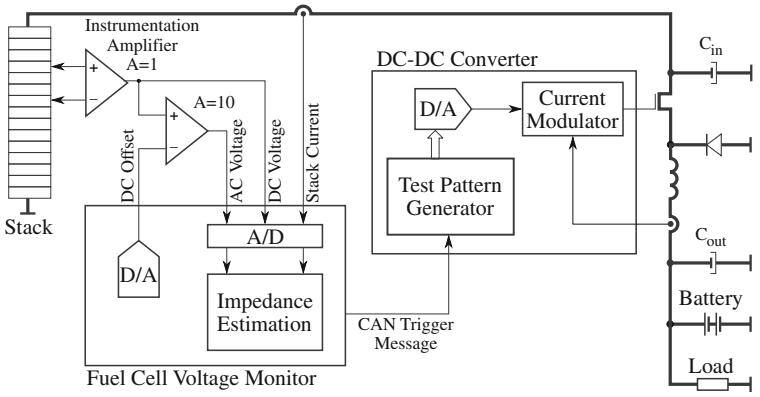

Fig. 7.10 Connection scheme between the FCVM and the DC-DC converter for online condition monitoring

7.3 Summary

The presented hardware components provide a platform for a versatile, online CM system. All things considered, such a CM system bridges the gap between the laboratory-grade measurement equipment and contemporary commercial diagnostic systems. The designed electronics use innovative design solutions by employing industry-standard components. Consequently, the constructed system is both (i) commercially viable and (ii) precise enough to perform sophisticated diagnostic measurements. The combination of the designed DC-DC converter with the 90-channel FCVM represents a capable platform for accurate online CM.

The system comprises a DC-DC converter with diagnostics capabilities, a 90-channel voltage monitor, and embedded algorithms for signal processing and condition monitoring. The developed DC-DC converter module can be grouped in parallel with what the overall output power is increased. Besides power conditioning, the DC-DC converter enables system probing with arbitrary signals that can be used for diagnostic purposes. Together with the FCVM, it provides the basic hardware platform for online condition monitoring of various types of electrochemical devices. Both devices are built to meet tight requirements regarding size and costs imposed by commercially oriented applications and at the same time to fulfil accuracy requirements set by the diagnostic methodology.

References

1. Wai, Rong Jong, Chung You Lin, Rou Yong Duan, and Yung Ruei Chang. 2007. High-efficiency DC-DC converter with high voltage gain and reduced switch stress. *IEEE Transactions on Industrial Electronics* 54 (1): 354–364. doi:10.1109/TIE.2006.888794.

2. Harfman Todorovic, M., L. Palma, and P.N. Enjeti. 2008. Design of a wide input range DC-DC converter with a robust power control scheme suitable for fuel cell power conversion. *IEEE Transactions on Industrial Electronics* 3: 1247–1255. doi:10.1109/TIE.2007.911200.
3. Wu, G., X. Ruan, and Z. Ye. 2015. Non-isolated high step-up DC-DC converters adopting switched-capacitor cell. *IEEE Transactions on Industrial Electronics* 62 (1): 383–393. doi:10.1109/TIE.2014.2327000.
4. Xuewei, Pan, and A.K. Rathore. 2014. Novel bidirectional snubberless naturally commutated soft-switching current-fed full-bridge isolated DC/DC converter for fuel cell vehicles. *IEEE Transactions on Industrial Electronics* 61 (5): 2307–2315. doi:10.1109/TIE.2013.2271599.
5. Valdivia, V., A. Barrado, A. Lazaro, M. Sanz, D. Lopez del Moral, and C. Raga. 2014. Black-box behavioral modeling and identification of DC-DC converters with input current control for fuel cell power conditioning. *IEEE Transactions on Industrial Electronics* 61 (4): 1891–1903. doi:10.1109/TIE.2013.2267692.
6. Tseng, Kuo Ching, and Chi Chih Huang. 2014. High step-up high-efficiency interleaved converter with voltage multiplier module for renewable energy system. *IEEE Transactions on Industrial Electronics* 61 (3): 1311–1319. doi:10.1109/TIE.2013.2261036.
7. Hu, X., and C. Gong. 2015. A high gain input-parallel output-series DC/DC converter with dual coupled inductors. *IEEE Transactions on Power Electronics* 30 (3): 1306–1317. doi:10.1109/TPEL.2014.2315613.
8. Siwakoti, Y.P., Poh Chiang Loh, F. Blaabjerg, S.J. Andreasen, and G.E. Town. 2015. Y-source boost DC/DC converter for distributed generation. *IEEE Transactions on Industrial Electronics* 62 (2): 1059–1069. doi:10.1109/TIE.2014.2345336.
9. Tang, Yu., Dongjin Fu, Ting Wang, and Zhiwei Xu. 2015. Hybrid switched-inductor converters for high step-up conversion. *IEEE Transactions on Industrial Electronics* 62 (3): 1480–1490. doi:10.1109/TIE.2014.2364797.
10. Burany, Stephen, Ravi B Gopal, Norman A Freeman, and Stephane Masse. 2006. Method and apparatus for monitoring fuel cell voltages.
11. Ordonez, M., M.O. Sonnaillon, J.E. Quaicoe, and M.T. Iqbal. 2010. An embedded frequency response analyzer for fuel cell monitoring and characterization. *IEEE Transactions on Industrial Electronics* 57 (6): 1925–1934. doi:10.1109/TIE.2009.2028295.
12. Skvarenina, Timothy L (ed.). 2001. *The power electronics handbook*. Industrial electronics. Boca Raton: CRC Press.
13. Kester, Walter Allan. 1998. *Analog devices practical design techniques for power and thermal management, analog devices technical reference books*. Norwood: Analog Devices.
14. Modulated constant off-time control mechanism, application note. Linfinity Microelectronics.
15. Chee, San Hwa. 1995. *A new, high efficiency monolithic buck converter*. Linear Technology.
16. Webb, Daniel, and Steffen Møller-Holst. 2001. Measuring individual cell voltages in fuel cell stacks. *Journal of Power Sources* 103: 54–60.
17. Brunner, Doug, Ajay K. Prasad, Suresh G. Advani, and Brian W. Peticolas. 2010. A robust cell voltage monitoring system for analysis and diagnosis of fuel cell or battery systems. *Journal of Power Sources* 195 (24): 8006–8012. doi:10.1016/j.jpowsour.2010.06.054.
18. Dobkin, Bob, and Jim Williams (eds.). 2011. *Analog circuit design - a tutorial guide to applications and solutions*. Amsterdam: Elsevier.

Chapter 8
Conclusion

EIS is a well established technique for the characterisation of electrochemical devices. However, conventional EIS approaches have two main deficiencies: (i) a long measurement time due to usage of naïve excitation signals, for instance (multi-)sine signals, and (ii) suboptimal signal processing algorithms that provide only time averaged impedance values. These two deficiencies are the main limiting factors that diminish the applicability of the conventional EIS technique for online condition monitoring of electrochemical devices. The fast EIS technique presented in this book addresses the aforementioned issues with the following improvements:

- the employment of a broad-band excitation signal,
- a time-frequency analysis technique, and
- specifying the statistical properties of the impedance values in closed form.

The fast EIS technique employs a DRBS waveform as an excitation signal, where the impedance is computed through CWT with Morlet mother wavelet. The combination of the DRBS excitation and the CWT signal processing enables timely measurements and provides high time-frequency resolution of the impedance results. The main advantage of the approach, compared to the conventional one, is shorter probing time thus decreasing the invasivity level subjected to the electrochemical device under test.

Performance of the fast EIS depends on two parameters: the DRBS bandwidth and Morlet wavelet central frequency. These values can be determined in a systematic manner, which guarantees optimal performance of the fast EIS technique.

The employed time-frequency analyses provides richer information about the measured impedance. Unlike the conventional frequency domain based approaches, which provide only time-averaged impedance values, the fast EIS technique allows thorough statistical analysis. As a result, statistical properties of the impedance values can be derived in a closed form due to the properties of the DRBS signal. Being

P. Boškoski et al., *Fast Electrochemical Impedance Spectroscopy*,
SpringerBriefs in Applied Sciences and Technology,
DOI 10.1007/978-3-319-53390-2_8

a random signal, the spectral components of the DRBS are complex circular random variables. These statistical properties are preserved within CWT coefficients. Therefore, the corresponding PDFs and CDFs of the impedance can be derived as a ratio of two complex circular random variables.

The fast EIS, performed together with the statistical analysis, is a suitable tool for online condition monitoring of electrochemical devices. Having derived the CDFs and PDFs of impedance components, the alarm thresholds for a CM system can be specified based on the desired probability of false alarm. The benefits of this process are twofold. First, the problem of alarm thresholds tuning is solved analytically. Secondly, PFA based threshold tuning is performed using data collected solely under fault-free operation. This removes the requirement for characterisation of the electrochemical device behaviour under various fault modes. As a result, the commissioning phase of a CM system is significantly simplified.

Based on the derived CDFs, a unit-free CI is specified. It reflects the departure of the particular impedance component from its reference value. This indicator serves as a broad indication of the state-of-health of an electrochemical device. The unit-free CI is constructed from a set of impedance values at various frequencies. It is derived as a result of an information aggregation process performed by copula functions, where the CI itself is defined as the output of the copula. The proposed CI describes the probability of observing a particular combination of the impedance values with respect to the reference ones. Thus, the value of the proposed CI is directly related to the condition of the electrochemical device as well as to the severity of the present fault.

The fast EIS technique was evaluated on RC circuits in simulation and with real measurements, as well as on several types of electrochemical devices:

- an industrial-grade 20 A h Li-ion battery,
- a laboratory-grade Li-S cell, and
- an 8.5 kW PEM fuel cell system.

The results confirm the applicability of the fast EIS technique for impedance measurement of various types of electrochemical devices. Furthermore, the performance of the CM system based on the fast EIS technique is shown to be sufficiently accurate when detecting various faults occurring in PEM fuel cell systems.

A detailed hardware description of a CM system for a PEM fuel cell system is included. The hardware setup consists of a modular DC-DC converter and 90-channel FCVM. Such a configuration enables joint injection of excitation signals and acquisition of measurements that are required for an impedance measurement. The systems bridges the gap between the laboratory-grade measurement equipment and the commercial diagnostic systems. It is both commercially viable and accurate enough to perform the measurements required for diagnostic purposes.

Appendix A
Listings

Listing A.1 Generation of the DRBS excitation

```
fs = 100000;
t = 0:1/fs:10-1/fs;

w = 2*pi*100;
s = sin(w*t);

u = [];
N = 100;
fs = 100000;
f_prbs = fs/N

for idx = 1:9999
    x = round(rand);
    if x == 0
        x = -1;
    end
    u( (idx-1)*N+1 : idx*N) = x;
end
```

Listing A.2 Simulation of the RC circuit

```
s = u;
t = (0:length(u)-1)/fs;
R = 1000 %Ohm
C = 1e-6 %Farads
Z = R/(R*C*j*w+1)
phi = angle(Z)
sX = abs(Z)*sin(w*t+phi);
sys = tf([R], [R*C, 1])
y = lsim(sys, s, t);
```


P. Boškoski et al., *Fast Electrochemical Impedance Spectroscopy*,
SpringerBriefs in Applied Sciences and Technology,
DOI 10.1007/978-3-319-53390-2

Listing A.3 Impedance characteristics via CWT

```
c_freq=logspace(0,1,20);
for qq=1:length(c_freq)
    f0 = 2*pi*c_freq(qq);
    MorletFourierFactor = 4*pi/(f0+sqrt(2+f0^2));

    f_max = 333;
    f_min = 1;

   WAV={'morl0',f0};

    nb = 15;
    s0 = 1/(f_max * MorletFourierFactor);
    mx = 1/(f_min * MorletFourierFactor);
    ds = log(mx/s0)/log(2)/(nb-1);
    scales = struct('s0',s0,'ds',ds,'nb',nb,'type','pow','pow',2);

    cwi = cwtft({s,1/fs},'wavelet',WAV,'scales',scales);
    cwu = cwtft({y,1/fs},'wavelet',WAV,'scales',scales);

    for ii=1:size(cwi.cfs,1)
        cws = cwi.cfs(ii,:);
        cwy = cwu.cfs(ii,:);
        cwz = cwy./cws;
        [rr, ss1, ss2]=estimate_pdf(cwy, cws );
        Zh = conj(rr)*ss1/ss2;
        w = 2*pi*cwi.frequencies(ii);
        Z = R/(R*C*i*w+1);
        r_rat(qq,ii) = real(Zh)/real(Z);
        i_rat(qq,ii) = imag(Zh)/imag(Z);
    end
    disp(c_freq(qq));
end
```

Listing A.4 Simulation of the cascade RC circuit

```
s = u;
t = (0:length(u)-1)/fs;
R1 = 1000 %Ohm
C1 = 1e-6 %Farads
R2 = 1000 %Ohm
C2 = 1e-6 %Farads
Z = R1/(R1*C1*j*w+1) + R2/(R2*C2*j*w+1);
phi = angle(Z)
sX = abs(Z)*sin(w*t+phi);
sys = tf([R], [R*C, 1])
y = lsim(sys, s, t);
```

Listing A.5 Estimation of PDF according to (3.13)

```
function [new_rho,s1,s2]=estimate_pdf(u_cof, i_cof)
x=u_cof;
y=i_cof;
z=u_cof./i_cof;
C=[mean(x.*conj(x)) mean(y.*conj(x)); ...
    mean(x.*conj(y)) mean(y.*conj(y))];
rho = C(1,2)/sqrt(C(1,1))/sqrt(C(2,2));
s1 = sqrt(C(1,1));
s2 = sqrt(C(2,2));

sx=s1;
sy=s2;

r=abs(z);
new_rho = fminsearch(@(xx) mle_ray_rat(xx, r, s2, s1), 0);
rho_r=-imag(rho)+1i*(-1)*real(rho);
new_rho = rho;
```

Listing A.6 Support function for maximum likelihood estimation of parameters for (3.13)

```
function mle = mle_ray_rat(rho, r, s1, s2)
    N = length(r);

    if rho>1 || rho<-1
        mle = inf;
    else
        mle = N*log(2) + N*log( (s1*s2*(1-rho^2))^2) + sum(log(r)
            )+ sum(log(s1^2*r.^2 + s2^2)) - ...
            (1/2)*sum( log( ((s1^2*r.^2 + s2^2).^2 - 4*rho^2*s1
                ^2*s2^2*r.^2).^3 ));
        mle = -sum(log(2*(1-rho^2)*(s1*s2)^2.*r.*(s1^2*r.^2+s2^2)
            ./sqrt(((s1^2*r.^2+s2^2).^2 - 4*rho^2*s1^2*s2^2*r.^2)
            .^3)));
    end
```